

A probabilistic, data-driven closure model for RANS simulations with aleatoric, model uncertainty

Atul Agrawal^a, Phaedon-Stelios Koutsourelakis^{a,b,*}

^a*Technical University of Munich, Professorship of Data-driven Materials Modeling, School of Engineering and Design, Boltzmannstr. 15, 85748 Garching, Germany*

^b*Munich Data Science Institute (MDSI - Core member), Garching, Germany*

Abstract

We propose a data-driven, closure model for Reynolds-averaged Navier-Stokes (RANS) simulations that incorporates aleatoric, model uncertainty. The proposed closure consists of two parts. A parametric one, which utilizes previously proposed, neural-network-based tensor basis functions dependent on the rate of strain and rotation tensor invariants. This is complemented by latent, random variables which account for aleatoric model errors. A fully Bayesian formulation is proposed, combined with a sparsity-inducing prior in order to identify regions in the problem domain where the parametric closure is insufficient and where stochastic corrections to the Reynolds stress tensor are needed. Training is performed using sparse, indirect data, such as mean velocities and pressures, in contrast to the majority of alternatives that require direct Reynolds stress data. For inference and learning, a Stochastic Variational Inference scheme is employed, which is based on Monte Carlo estimates of the pertinent objective in conjunction with the reparametrization trick. This necessitates derivatives of the output of the RANS solver, for which we developed an adjoint-based formulation. In this manner, the parametric sensitivities from the differentiable solver can be combined with the built-in, automatic differentiation capability of the neural network library in order to enable an end-to-end differentiable framework. We demonstrate the capability of the proposed model to produce accurate, probabilistic, predictive estimates for all flow quantities, even in regions where model errors are present, on a separated flow in the backward-facing step benchmark problem.

Keywords: data-driven turbulence modeling, Reynolds-Averaged Navier-Stokes, uncertainty quantification, deep neural networks, differentiable solver

1. Introduction

Turbulence is ubiquitous in fluid flows and of importance to a vast range of applications such as aircraft design, climate and ocean modeling. It has challenged and intrigued scientists and artists for centuries [1]. In the context of the Navier-Stokes equations, the most accurate numerical solution strategy for turbulent flows is offered by Direct Numerical Simulation (DNS),

*Corresponding author

Email addresses: atul.agrawal@tum.de (Atul Agrawal), p.s.koutsourelakis@tum.de (Phaedon-Stelios Koutsourelakis)

Preprint submitted to Journal of Computational Physics

April 16, 2024

which aims at fully resolving all scales of motion. While this simulation method yields impeccable results, it is prohibitively expensive in terms of computational cost due to the very fine discretizations needed which scale as $O(\text{Re}^{11/4})$ [2]. Reynolds-averaged Navier-Stokes (RANS) models offer a much more efficient alternative for predicting mean flow quantities. They represent the industry standard which is expected to remain the case in the coming decades [3]. Their predictive accuracy however hinges upon the closure model adopted.

The greater availability of computational resources and the development of scalable learning frameworks in the field of machine learning have had a significant impact in computational fluid mechanics as well [4, 5, 6]. Data-driven closures for RANS have revitalized turbulence modeling [7], and a comprehensive reviews can be found in [8, 4]. The construction of such closure models consists of two steps: (i) postulating a model form ansatz; and (ii) fitting/learning/infering model parameters on the basis of the available data. Pertinent approaches have focused on learning model coefficients of a given turbulence model [9] (often with statistical inference), on modeling of correction or source terms for an existing turbulence model [10, 11, 12, 13, 14] and on directly modeling the Reynolds stress (RS) tensor [15, 16, 17, 18] with symbolic regression [19] or neural networks [15, 17, 20] or Gaussian Processes [14] or Random Forests [16, 18]. Of particular relevance to the present study is the work of [15] wherein they use the non-linear eddy viscosity model (NLEVM) [21] to capture the anisotropic part of the RS tensor using an integrity tensor basis and a deep neural network employing local, invariant flow features. This model owing to its guaranteed Galilean invariance found a wider utilization [17, 22, 20].

In most of the methods discussed above, data-based training is performed in a *non-intrusive* manner, i.e., without involving the RANS solver in the training process. The major shortcomings of such a strategy (which we attempt to address in the present paper) are two-fold. Firstly inconsistency issues, which can arise between the data-driven model and the baseline turbulence model (e.g., $k - \epsilon$) [23, 7]. [24] showed that even substituting RS fields from reputable DNS databases may not lead to satisfactory prediction of the velocity field, and [25] investigated the ill-conditioning that arises in the RANS equations, when employing data-driven models that treat the Reynolds stress as an explicit source term. This ill-conditioning can be amplified within each iteration, thus potentially leading to divergence during the solution procedure. Secondly, such models rely on full-field Reynolds stress training data, which are only available when high-fidelity simulations such as DNS/Large-Eddy Simulations (LES) are used. Unfortunately, such high-fidelity simulations due to their expense are limited to simple geometries and low Reynolds numbers.

In order to address these limitations, we advocate incorporating the RANS model in the training process. This enables one to use indirect data (e.g., mean velocities and pressure) obtained from higher-fidelity simulations or experiments as well as direct data (i.e. RS tensor observables) if this is available. In the subsequent discussions, we will refer to such a training strategy as "model-consistent learning" [7]. It necessitates the solution of a high-dimensional inverse problem that minimizes a discrepancy measure between the RANS solver's output (mean velocities and pressure) and the observables (e.g. mean fields from LES/DNS). As pointed out in [7], model-consistent training or simulation-based Inference [26] benefits from the differentiability of the solver, as it provides derivatives of the outputs with respect to the tunable parameters that can significantly expedite the learning/inference process.

In recent years there has been a concerted effort towards developing differentiable CFD solvers [27, 28, 29, 30] in Auto-Differentiation (AD) enabled modules like PyTorch, TensorFlow, JAX, Julia. To the best of the authors' knowledge, this has not been accomplished yet for RANS solvers. One way to enable the computation of parametric sensitivities is by developing

adjoint solvers [31, 32], which are commonly used in the context of aerodynamic shape optimization [33]. Such adjoint-based modules have also been employed to infer a spatial, corrective field for transport equations [34, 10, 11] and Reynolds stresses [13]. Recently, [35, 36] tried to learn a corrective, multiplicative field in the production term of the Spalart–Allmaras transport model. This is based on an alternative approach outlined in [10], in which empirical correction terms for the turbulence transport equations are learned while retaining a traditional linear eddy viscosity model (LEVM) for the closure. [37] used adjoints to recover a spatially varying eddy viscosity correction factor from sparsely distributed training data, but they also retained the LEVM assumption. More recently, researchers performed model-consistent or CFD-driven training by involving the solver in the training process. [38, 39] used gradient-free algorithms to perform symbolic identification of the explicit algebraic Reynolds stress models (ARSM) , [40] (with adjoint methods) and [20] (with ensemble methods) combined the RANS solver and a NLEVM-based neural network proposed by [15] in order to learn the model closure. However, they did not account for potential model errors in the closure equation which may arise due to the reasons discussed in the next paragraph.

We argue that even in model-consistent training, a discrepancy in the learnt RS closure model can arise due to the fact that a) the parametric, functional form employed may be insufficient to represent the underlying model¹, and b) the flow features which are used as input in the closure relation and which are generally restricted to each point in the problem domain (locality/Markovianity assumption [41]), might not contain enough information to predict the optimal RS tensor leading to irrecoverable loss of information. Hence irrespective of the type and amount of training data available, there could be *aleatoric* uncertainty in the closure model that needs to be quantified and propagated in the predictive estimates. We note that much fewer efforts have been directed towards quantifying uncertainties in RANS turbulence models. Earlier, parametric approaches broadly explored the uncertainties in the model choices [9] (i.e., uncertainty involved in choosing the best model among a class of competing models, e.g., $k - \omega, k - \epsilon$) and their respective model coefficients [42]. Recently the shortcomings of the parametric closure models have been recognized by the turbulence modeling community [43, 44]. In light of this, various non-parametric approaches have targeted model-form uncertainty whereby uncertainties are directly introduced into the turbulent transport equations or the modeled terms such as the Reynolds stress [22] or eddy viscosity. Such formulations allow for more general estimates of the model inadequacy than the parametric approaches. Researchers have also tried perturbing the eigenvalues [45, 46, 47], transport eigenvectors [48] or the tensor invariants. [49] used kernel density estimates to predict the confidence of data-driven models, but it is limited to the prediction of the anisotropic stress and fails to provide any probabilistic bounds. [22] tries to address this issue by incorporating a Bayesian formulation in order to quantify epistemic uncertainty and then propagating it to quantities of interest like pressure and velocity. For a comprehensive review of modeling uncertainties in the RANS models the reader is directed to [43].

In order to address the aforementioned limitations, we propose a novel probabilistic, model-consistent, data-driven differential framework. The framework enables learning of a NLEVM-based, RS model in a model-consistent way using a differentiable RANS solver, with mean field observables (velocities and/or pressure). To the authors’ knowledge, uncertainty quantification has not been addressed for data-driven turbulence model training with indirect observations. We

¹For example the models based on the Boussinesq hypothesis will fail to capture the flow features driven by the anisotropy of the Reynolds stresses and this intrinsic deficiency cannot be remedied by the calibration of the model coefficients with data.

propose to augment the parametric closure model of the RS tensor by a stochastic discrepancy tensor to quantify model errors at different parts of the problem domain. With the introduction of the stochastic discrepancy tensor, we advocate a probabilistic formulation for the associated inverse problem, which provides a superior setting as it is capable of quantifying predictive uncertainties which are unavoidable when any sort of model/dimensionality reduction is pursued and when the model (or its closure) is learned from finite data [50]. To achieve the desired goals, the proposed framework employs the following major elements:

- A discrete, adjoint-based differentiable RANS solver to enable model-consistent, gradient-based learning (Section (2.2), Section (2.2.4)).
- The RS closure model consists of a parametric part that is expressed with an invariant neural network as proposed in [15] (Section (2.2.1)), to which a *stochastic* discrepancy tensor field is added in order to account for the insufficiency of the parametric part (Section (2.2.2)).
- A fully Bayesian formulation that enables the quantification of epistemic uncertainties and their propagation to the predictive estimates (Section (2.2.4), Section (2.2.5))
- This is combined with a *sparsity-inducing* prior model that activates the discrepancy term only in regions of the problem domain where the parametric model is insufficient (Section (2.2.2)).

The structure of the rest of the paper is as follows. Section (2) presents the governing equations and their discretization, the closure model proposed consisting of the parametric part and the stochastic corrections provided by latent variables introduced. We also present associated prior and posterior densities, a stochastic Variational Inference scheme that was employed for identifying model parameters and variables as well as the computation of predictive estimates with the trained model. Finally, Section (3) discusses the implementation aspects and demonstrates the accuracy and efficacy of the proposed framework in the backward-facing step test case [51], where the linear eddy viscosity models are known to fail. We compare our results with LES reference values and the $k - \epsilon$ model, which is arguably the most commonly used RANS model. In Section (4), we summarize our findings and discuss limitations and potential enhancements.

2. Methodology

2.1. Problem Statement

2.1.1. Reynolds-Averaged Navier-Stokes (RANS) equations

The Navier-Stokes equations for incompressible flows of Newtonian fluids are given by (in indicial notation):

$$\frac{\partial U_i}{\partial t} + \frac{\partial}{\partial x_j}(U_i U_j) = \nu \frac{\partial^2 U_i}{\partial x_j \partial x_j} - \frac{1}{\rho} \frac{\partial P}{\partial x_i}, \quad (1)$$

$$\frac{\partial U_j}{\partial x_j} = 0, \quad (2)$$

where i, j are free and dummy indices respectively taking values 1, 2, 3 and U_i, P, t, x_j, ν and ρ represent the flow velocity, pressure, time, spatial coordinates, the dynamic viscosity and the

density of the fluid respectively. The non-linearity of the convective term $\frac{\partial}{\partial x_j}(U_i U_j)$ gives rise to chaotic solutions beyond a critical value of the *Reynolds number* Re . This necessitates very fine spatio-temporal discretizations in order to capture the salient scales. Such brute-force, fully-resolved simulations, commonly referred to as Direct Numerical Simulations (DNS), can become prohibitively expensive, particularly as Re increases.

The velocity field can be decomposed into its time-averaged (or mean) part u and the part corresponding, to generally fast, fluctuations \tilde{u} as:

$$U_i(\mathbf{x}, t) = u_i(\mathbf{x}) + \tilde{u}_i(\mathbf{x}, t), \quad (3)$$

$$\text{where, } u_i(\mathbf{x}) = \langle U_i(\mathbf{x}, t) \rangle = \lim_{T \rightarrow \infty} \frac{1}{T} \int_0^T U_i(\mathbf{x}, t) dt. \quad (4)$$

Similarly the pressure field is also decomposed as

$$P(\mathbf{x}, t) = p(\mathbf{x}) + \tilde{p}(\mathbf{x}, t), \quad (5)$$

$$\text{where } p(\mathbf{x}) = \langle P(\mathbf{x}, t) \rangle = \lim_{T \rightarrow \infty} \frac{1}{T} \int_0^T P(\mathbf{x}, t) dt. \quad (6)$$

Substituting these decompositions into the Navier-Stokes equations (Equation (1)) and applying time-averaging results in the Reynolds-averaged Navier-Stokes (RANS) equations [2, 52], i.e.:

$$u_j \frac{\partial u_i}{\partial x_j} - \nu \frac{\partial^2 u_i}{\partial x_j \partial x_j} + \frac{1}{\rho} \frac{\partial p}{\partial x_i} = - \frac{\partial \langle \tilde{u}_i \tilde{u}_j \rangle}{\partial x_j}, \quad (7)$$

$$\frac{\partial u_i}{\partial x_i} = 0, \quad (8)$$

where $\langle \cdot \rangle$ denotes the time average of the arguments as in Equation (4) or Equation (6). In several engineering applications involving turbulent flows, the quantities of interest depend upon the time-averaged quantities. These can be obtained by solving the RANS equations which in general implies a much lower computational cost than DNS.

2.1.2. The closure problem

The RANS equations are unfortunately *unclosed* as they depend on the cross-correlation of the fluctuating velocity components, commonly referred to as the Reynolds-Stress (RS) tensor τ_{RS} :

$$\tau_{RS} = - \langle \tilde{u}_i \tilde{u}_j \rangle. \quad (9)$$

The goal of pertinent efforts is therefore to devise appropriate closure models where the RS tensor τ_{RS} is expressed as a function as the primary state variables in the RANS equations i.e. the time-averaged flow quantities. Closure models are of three types: (i) Functional, which use physical insight to construct the closure; (ii) Structural, which use mathematical tools; and (iii) Data-driven, which employ experimental/simulation data [53]. For a comprehensive review, the reader is directed to [54, 53, 55]. Classically, turbulence models are devised to represent higher-order moments of the velocity fluctuations in terms of lower-order moments. This can be done directly, as in the case of the eddy-viscosity models, or indirectly, as in the case of models based

on the solution of additional partial differential equations [2].

The most commonly employed strategy is based on the linear-eddy-viscosity-model (LEVVM), which uses the Boussinesq approximation according to which τ_{RS} is expressed as:

$$\tau_{LEVVM} = \frac{2}{3}k\mathbf{I} - 2\nu_t\bar{\mathbf{S}}, \quad (10)$$

where ν_t is the eddy viscosity, $\bar{\mathbf{S}} = \frac{1}{2}(\nabla\mathbf{u} + \nabla\mathbf{u}^T)$ is the mean strain-rate tensor, \mathbf{I} is the second order identity tensor, and $k = -\frac{1}{2}\text{tr}(\tau_{RS})$ is the turbulent kinetic energy. The eddy viscosity is computed after solving the equation(s) for the turbulent flow quantities such as the turbulent kinetic energy k and the turbulent energy dissipation ϵ (e.g. the $k - \epsilon$ model [56]), or the specific dissipation ω (e.g. the $k - \omega$ [57]). Although the Boussinesq approximation provides accurate results for a range of flows, it can give rise to predictive inaccuracies which are particularly prominent when trying to capture flows with significant curvatures, recirculation zones, separation, reattachment, anisotropy, etc [2, 58]. Attempts to overcome this weakness have been made in the form of nonlinear eddy viscosity models (e.g., [59, 21, 60]), Reynolds-stress transport models (e.g., [61]) and ARSM (e.g., [62, 63]). These models have not received widespread attention because they lack the robustness of LEVVM and involve more parameters that need to be calibrated.

2.2. Probabilistic, model-consistent data-driven differential framework

Upon discretisation using e.g. a finite element scheme (Appendix A), one can express the RANS equations (Equation (7)) in residual form as:

$$\mathcal{G}(\mathbf{z}) = \mathbf{B}\boldsymbol{\tau} \quad (11)$$

$$\text{or, } \mathcal{R}(\mathbf{z}; \boldsymbol{\tau}) := \mathcal{G}(\mathbf{z}) - \mathbf{B}\boldsymbol{\tau} = 0, \quad (12)$$

where $\mathbf{z} = [\mathbf{u}, p]^T$ summarily denotes the discretized velocity \mathbf{u} and pressure p fields and $\boldsymbol{\tau}$ the discretized RS field. E.g. for a two-dimensional flow domain $\mathbf{z} \in \mathbb{R}^{N \times 3}$, $\boldsymbol{\tau} \in \mathbb{R}^{N \times 3}$ where N is the number of grid points. The discretization scheme employed and other implementation details are discussed in Appendix A. We denote with \mathcal{G} the discretized, non-linear operator accounting for the advective and diffusive terms on the left-hand side of Equation (7) as well as the conservation of mass in Equation (8), and with \mathbf{B} the matrix (i.e. linear operator) arising from the divergence term on the right-hand side of Equation (7).

Traditional, data-driven strategies postulate a closure e.g. $\tau_\theta(\mathbf{z})$ (or most often $\tau_\theta(\mathbf{u})$) dependent on some tunable parameters θ , which they determine either by assuming that reference Reynolds-stress data is available from DNS simulations (or in general, from higher-fidelity models such as LES) or by employing experimental or simulation-based data of the mean velocities/pressures i.e. of \mathbf{z} . The former scenario which is referred to as *model regression* [64] has received significant attention in the past (e.g. [22, 15, 65, 17]). Apart from the heavier data requirements, it does not guarantee that the trained model would yield accurate predictions of \mathbf{z} [24] as even small errors in $\boldsymbol{\tau}$ might get amplified when solving Equation (12). The second setting, referred to as *trajectory regression* in [64], might be able to make use of indirect and noisy observations but is much more cumbersome as repeated model evaluations and parametric sensitivities, i.e. a differentiable solver, are needed for training.

Critical to any data-driven model is its ability to generalize i.e. to produce accurate predictions under different flow scenarios. On one hand this depends on the training data available

but on the other, on incorporating a priori available domain knowledge. The latter can attain various forms and certainly includes known invariances or equivariances that characterize the associated maps. Apart from this and the particulars of the parameterized model form, a critical aspect pertains to uncertainty quantification. We distinguish between parametric and model uncertainty. The former is of epistemic origin and has been extensively studied (e.g., [9, 42, 43]). Bayesian formulations offer a rigorous manner for quantifying it and ultimately propagating it in the predictive estimates in the form of the predictive posterior. We note however that in the limit of infinite data, the posterior of the model parameters θ (no matter what these are or represent) would collapse to a Dirac-delta i.e. point-estimates for θ would be obtained. This false lack of uncertainty does not imply that the model employed is perfect as the true (unknown) closure might attain a form not contained in the parametric family used or in the features of \mathbf{z} that appear in the input (e.g. even though all models proposed employ a locality assumption in the closure equations, non-local features of \mathbf{u} might be needed).

The issue of model uncertainty in the closure equations which is of an aleatoric nature, has been much less studied and represents the main contribution of this work. In particular, we augment the parametric closure model $\tau_\theta(\mathbf{u})$ with a set of latent (i.e. unobserved) random variables ϵ_τ which are embedded in the model equations and which quantify model discrepancies at each grid point. In reference to the discretized RS vector τ in Equation (12), we propose:

$$\tau = \tau_\theta(\mathbf{u}) + \epsilon_\tau. \quad (13)$$

We emphasize the difference between model parameters θ and the random variables ϵ_τ . While both are informed by the data, the latter remain random even in the limit of infinite data. As we explain in the sequel, we advocate a fully Bayesian formulation that employs indirect observations of the velocities/pressures. These are combined with appropriate sparsity-inducing priors which can turn-off model discrepancy terms when the parametric model is deemed to provide an adequate fit. In this manner, the regions of the problem domain where the closure is most problematic are identified while probabilistic, predictive estimates are always obtained. In particular, in Section (2.2.1) the parametric part of the closure model is discussed. In Section (2.2.2) the proposed, stochastic, discrepancy tensor is presented. In Section (2.2.3) prior and posterior densities are discussed and in Section (2.2.4) the corresponding inference and learning algorithms are introduced. Finally in Section (2.2.5), the computation of predictive estimates using the trained model is discussed.

2.2.1. Parametric RS model

In this section we discuss the parametric part, i.e. $\tau_\theta(\mathbf{u})$ in the closure model of Equation (13). As this represents a vector containing its values at various grid points over the problem domain, the ensuing discussion and equations should be interpreted as per grid point. We note that the most popular LEVM model (Equation (10)) assumes that the anisotropic part of the τ_{LEVM} , is linearly related to the mean strain rate tensor $\bar{\mathbf{S}}$. This linear relation assumption restricts the model to attain a small subset of all the possible states of turbulence. This subset is referred to as the plane strain line [66]. Experimental and DNS data show that turbulent flows explore large regions of the domain of realizable turbulence states.

In the present work, we make use of the invariant neural network architecture proposed by [15] which relates the anisotropic part of the RS tensor with the symmetric and antisymmetric components of the velocity gradient tensor. By using tensor invariants, the neural network is able to achieve both Galilean invariance as well as rotational invariance. The Navier-Stokes

equations are Galilean-invariant, i.e. they remain unchanged for all inertial frames of reference. The theoretical foundation of this neural network lies in the Non-Linear Eddy Viscosity Model (NLEVM) proposed by [21] and has been used in several studies [22, 13, 17]. By employing barycentric realizability maps [46, 45, 67, 66, 48], it was shown in [17] that this architecture overcomes the plane strain line restriction and can explore other realizable states.

In the model proposed by [21], the normalized anisotropic tensor of the R-S was given by $\mathbf{b} := \mathbf{b}(\mathbf{S}, \mathbf{\Omega})$, which was a function of the normalized mean rate of strain tensor \mathbf{S} and the rotation tensor $\mathbf{\Omega}$, i.e.:

$$\boldsymbol{\tau} = 2k\mathbf{b} + \frac{2k}{3}\mathbf{I}; \quad \mathbf{S} = \frac{1}{2} \frac{k}{\epsilon} (\nabla\mathbf{u} + \nabla\mathbf{u}^T) \quad \mathbf{\Omega} = \frac{1}{2} \frac{k}{\epsilon} (\nabla\mathbf{u} - \nabla\mathbf{u}^T). \quad (14)$$

Through the application of Cayley-Hamilton theorem [21], the following general expression for the anisotropy tensor \mathbf{b} was adopted:

$$\mathbf{b} = \sum_{k=1}^{10} G^{(k)}(\underbrace{\mathcal{I}_1 \dots \mathcal{I}_5}_{\substack{\text{Scalar} \\ \text{Invariants}}}) \mathcal{T}^{(k)}, \quad (15)$$

where:

$$\mathcal{I}_1 = \text{tr}(\mathbf{S}^2), \quad \mathcal{I}_2 = \text{tr}(\mathbf{\Omega}^2), \quad \mathcal{I}_3 = \text{tr}(\mathbf{S}^3), \quad \mathcal{I}_4 = \text{tr}(\mathbf{\Omega}^2\mathbf{S}), \quad \mathcal{I}_5 = \text{tr}(\mathbf{\Omega}^2\mathbf{S}^2), \quad (16)$$

and $\mathcal{T}^{(k)}$ are the symmetric tensor basis functions (the complete set is listed in Table 1). The coefficients $G^{(i)}$ are scalar, non-linear functions which depend on the five invariants $\mathcal{I}_1 \dots \mathcal{I}_5$ and must be determined. If $G^{(1)} = -0.09, G^{(n)} = 0$, the NLEVM degenerates to the classical $k - \epsilon$ model. When the NLEVM was proposed, it was impossible to find good approximations for these functions and as a result, it did not receive adequate attention. This hurdle however was overcome with the help of machine learning [15] where $G^{(i)}$ were learned from high-fidelity simulation data. Neural networks with parameters $\boldsymbol{\theta}$ were employed for the coefficients i.e. $G_{\boldsymbol{\theta}}^{(i)}$ and:

$$\mathbf{b}_{\boldsymbol{\theta}} = \sum_{i=1}^{10} G_{\boldsymbol{\theta}}^{(i)}(\underbrace{\mathcal{I}_1 \dots \mathcal{I}_5}_{\substack{\text{Scalar} \\ \text{Invariants}}}) \mathcal{T}^{(i)}; \quad \boldsymbol{\tau}_{\boldsymbol{\theta}} = 2k\mathbf{b}_{\boldsymbol{\theta}} + \frac{2k}{3}\mathbf{I}. \quad (17)$$

We use $\boldsymbol{\tau}_{\boldsymbol{\theta}}$ to denote the neural-network-based, discretized RS tensor terms in the subsequent discussions.

As in [22], we employ the following prior for the NN parameters $\boldsymbol{\theta}$:

$$p(\boldsymbol{\theta} | \nu) = \mathcal{N}(\boldsymbol{\theta} | 0, \nu^{-1} \mathbf{I}_{d_{\boldsymbol{\theta}}}), \quad p(\nu) = \text{Gamma}(\nu | a_0, b_0), \quad (18)$$

where $d_{\boldsymbol{\theta}} = \text{dim}(\boldsymbol{\theta})$ and a Gamma hyperprior was used for the common precision hyperparameter ν with $(a_0, b_0) = (1.0, 0.02)$. The resulting prior has the density of a Student's \mathcal{T} -distribution centered at zero, which is obtained by analytically marginalizing over the hyperparameter ν [68].

Similarly however to the most widely used RANS closure models, such as the Launder-Sharma $k - \epsilon$ [56] or Wilcox's $k - \omega$ [57], which are based on the Boussinesq turbulent-viscosity hypothesis, the present model of $\boldsymbol{\tau}_{\boldsymbol{\theta}}$ postulates that the RS tensor at each point in the problem

$\mathcal{T}^{(1)} = \mathbf{S},$	$\mathcal{T}^{(6)} = \mathbf{\Omega}^2 \mathbf{S} + \mathbf{S} \mathbf{\Omega}^2 - \frac{2}{3} \text{tr}(\mathbf{S} \mathbf{\Omega}^2) \mathbf{I},$
$\mathcal{T}^{(2)} = \mathbf{S} \mathbf{\Omega} - \mathbf{\Omega} \mathbf{S},$	$\mathcal{T}^{(7)} = \mathbf{\Omega} \mathbf{S} \mathbf{\Omega}^2 + \mathbf{\Omega}^2 \mathbf{S} \mathbf{\Omega},$
$\mathcal{T}^{(3)} = \mathbf{S}^2 - \frac{1}{3} \text{tr}(\mathbf{S}^2) \mathbf{I},$	$\mathcal{T}^{(8)} = \mathbf{S} \mathbf{\Omega} \mathbf{S}^2 - \mathbf{S}^2 \mathbf{\Omega} \mathbf{S},$
$\mathcal{T}^{(4)} = \mathbf{\Omega}^2 - \frac{1}{3} \text{tr}(\mathbf{\Omega}^2) \mathbf{I},$	$\mathcal{T}^{(9)} = \mathbf{\Omega}^2 \mathbf{S}^2 + \mathbf{S}^2 \mathbf{\Omega}^2 - \frac{2}{3} \text{tr}(\mathbf{S}^2 \mathbf{\Omega}^2) \mathbf{I},$
$\mathcal{T}^{(5)} = \mathbf{\Omega} \mathbf{S}^2 - \mathbf{S}^2 \mathbf{\Omega},$	$\mathcal{T}^{(10)} = \mathbf{\Omega} \mathbf{S}^2 \mathbf{\Omega}^2 - \mathbf{\Omega}^2 \mathbf{S}^2 \mathbf{\Omega},$

Table 1: Complete set of basis tensors $\mathcal{T}^{(n)}$, that can be formed from \mathbf{S} and $\mathbf{\Omega}$. Matrix notation is used for clarity. The trace of a tensor is denoted by $\text{tr}(\mathbf{S}) = S_{ii}$.

domain depends on the flow features at the same point (locality assumption). This is a very strong assumption for flows that exhibit strong inhomogeneity [2].

2.2.2. Stochastic discrepancy term to RS

We argue that despite the careful selection of input features of the mean velocity field and the flexibility in the resulting map afforded by the NN architecture, the final form might not be able to accurately capture the true RS or at least not at every grid point in the problem domain. This would be the case, if e.g. non-local terms, which are unaccounted in the aforementioned formulation, played a significant role. As mentioned earlier, this gives rise to model uncertainty of an aleatoric nature which is of a different type than the epistemic uncertainty in the parameters θ of the closure model presented in the previous section. It is this model uncertainty that we propose to capture with the latent, random vector ϵ_τ in Equation (13). As for τ_θ in the previous section, ϵ_τ is a vector containing the contribution from all grid points in the problem domain. Hence, in the two-dimensional setting and given the symmetry of the RS tensor, ϵ_τ would be of dimension $d_\epsilon = 3N$ where N is the total number of grid points.

Before discussing the prior specification for ϵ_τ and associated inference procedures, we propose a dimension-reduced representation that would facilitate subsequent tasks given the high values that N takes in most simulations. In particular, we represent ϵ_τ as:

$$\epsilon_\tau = \mathbf{W} \mathbf{E}_\tau. \quad (19)$$

It is based on considering N_d subdomains of the problem domain and assuming that for all grid points in a certain subdomain, the corresponding RS discrepancy terms are identical. This can be expressed as in Equation (19) above where the entries of \mathbf{W} are 1 if a corresponding grid point (row of \mathbf{W}) belongs in a certain subdomain (column of \mathbf{W}) and 0 otherwise. A non-binary \mathbf{W} would also be possible, although in this case its physical interpretation in terms of subdomains would be occluded. The vector $\mathbf{E}_\tau = \{\mathbf{E}_{\tau,j}\}_{j=1}^{N_d}$ contains therefore the RS discrepancy terms for each subdomain, e.g. $\dim(\mathbf{E}_{\tau,j}) = 3$ for a two-dimensional flow. The dimensionality reduction scheme resembles Principal Component Analysis (PCA) [69]. In contrast to the latter however, we never have data/observations of the vectors to be reduced, i.e. ϵ_τ in our case. These are inferred implicitly from the LES data and simultaneously with \mathbf{W} . In the ensuing numerical illustrations, the division into subdomains is done in a regular manner and \mathbf{W} is prescribed a priori. One could nevertheless readily envision a learnable \mathbf{W} or even an adaptive refinement into subdomains.

The incorporation of the model discrepancy variables ϵ_τ or \mathbf{E}_τ at each grid-point or subdomain introduces redundancies i.e. there would be an infinity of combinations of θ and $\epsilon_\tau/\mathbf{E}_\tau$ that

could fit the data equally well. In order to address this issue, we invoke the concept of *sparsity* which has been employed in similar situations in the context of physical modeling [70, 71]. To this end, we make use of a sparsity-enforcing Bayesian prior based on the Automatic Relevance Determination (ARD) [72, 73]. In particular:

$$p(\mathbf{E}_\tau|\mathbf{\Lambda}) = \prod_{J=1}^{N_d} p(\mathbf{E}_{\tau,J}|\mathbf{\Lambda}^{(J)}) = \prod_{J=1}^{N_d} \mathcal{N}(\mathbf{E}_{\tau,J} | \mathbf{0}, \text{diag}(\mathbf{\Lambda}_J)^{-1}), \quad (20)$$

where $\mathbf{E}_{\tau,J}$ denotes the stochastic RS discrepancy term at subdomain J and the vector of hyperparameters $\mathbf{\Lambda}_J$ contains the corresponding precisions (e.g. for two-dimensional flows, $\text{dim}(\mathbf{\Lambda}_J) = 3$). A-priori therefore we assume that the RS discrepancies are zero on average with an unknown variance/precision that will be learned from the data as it will be discussed in the sequel. This is combined with the following hyperprior (omitting the hyperparameters α_0, β_0):

$$p(\mathbf{\Lambda}) = \prod_{J=1}^{N_d} \prod_{\ell=1}^L \text{Gamma}(\Lambda_{J,\ell} | \alpha_0, \beta_0), \quad (21)$$

where $\Lambda_{J,\ell}$ denotes the ℓ^{th} entry (e.g. $L = 3$ for two-dimensional flows) of the vector of precision hyperparameters in subdomain J . We note that when $\Lambda_{J,\ell} \rightarrow \infty$, then the corresponding model discrepancy term $E_{\tau,J,\ell} \rightarrow 0$. The resulting prior for \mathbf{E}_τ arising by marginalizing the hyperparameters $\mathbf{\Lambda}$ is a light-tailed, Student's t-distribution [74] that promotes solutions in the vicinity of 0 unless strong evidence in the data suggests otherwise. The hyperparameters α_0, β_0 are effectively the only ones that need to be provided by the analyst. We advocate very small values ($\alpha_0 = \beta_0 = 10^{-3}$ was used in the ensuing numerical illustrations) which correspond to an uninformative prior [75]. This is consistent with the values adopted in the original paper where the ARD prior was employed in conjunction with variational inference i.e. in [75].

The dimension of the ϵ_τ is high i.e. $3N$ in 2D (and $6N$ in 3D) where N is the total number of grid points. In contrast, the dimension of θ is independent of the grid as the parametric part of the closure model is the same at all grid points. Depending on the amount of data, one can envision cases where multiple combinations of ϵ_τ and θ could fit the data equally well. Non-zero values of ϵ_τ would imply model errors at the corresponding grid points. Ceteris paribus, we would prefer the combination with the least number of model errors or equivalently the one for which our parametric model can capture for most of the domain the closure accurately. It is indeed these types of solutions/combinations that the ARD prior promotes.

2.2.3. Data, likelihood and posterior

The probabilistic model proposed is trained with *indirect* observational data that pertain to time-averaged velocities and pressures at various points in the problem domain. This is in contrast to the majority of efforts in data-driven RANS closure modeling [22, 15, 65, 17], which employ *direct* RS data. In the ensuing numerical illustrations, the data is obtained from higher-fidelity computational simulations, but one could readily make use of actual, experimental observations.

In particular, we consider $M \geq 1$ flow settings and denote the observations collected as $\mathcal{D} = \{\hat{\mathbf{z}}^{(m)}\}_{m=1}^M$. These consist of time-averaged velocity/pressure values where $\text{dim}(\hat{\mathbf{z}}^{(m)}) = N_{\text{obs}}$. The locations of these measurements do not necessarily coincide with the mesh used to solve the RANS model in Equation (7) nor is it necessary that the same number of observations is available

for each of the M flow settings. The data is ingested with the help of a Gaussian likelihood:

$$\begin{aligned} p(\mathcal{D} | \boldsymbol{\theta}, \boldsymbol{\epsilon}_\tau^{(1:M)}) &= \prod_{m=1}^M p(\hat{\mathbf{z}}^{(m)} | \boldsymbol{\theta}, \boldsymbol{\epsilon}_\tau^{(m)}) \\ &= \prod_{m=1}^M \mathcal{N}(\hat{\mathbf{z}}^{(m)} | \mathbf{z}(\boldsymbol{\theta}, \boldsymbol{\epsilon}_\tau^{(m)}), \boldsymbol{\Sigma}), \end{aligned} \quad (22)$$

where $\mathbf{z}(\boldsymbol{\theta}, \boldsymbol{\epsilon}_\tau^{(m)})$ denotes the solution vector of the discretized RANS equations (see Equation (7)) with the closure model suggested by Equation (13) i.e. $\boldsymbol{\tau} = \boldsymbol{\tau}_\theta(\mathbf{u}) + \boldsymbol{\epsilon}_\tau^{(m)}$. We note that a different set of latent variables $\boldsymbol{\epsilon}_\tau^{(m)}$ is needed for each flow scenario as, by its nature, model discrepancy will in general assume different values under different flow conditions. We also note that the $\boldsymbol{\epsilon}_\tau$ is grid-dependent or problem geometry-dependent, which restricts it from making predictions for a completely different flow geometry. One could, with appropriate modeling enhancements, learn the dependence of $\boldsymbol{\epsilon}_\tau$ on flow parameters (e.g. boundary/initial conditions, geometry, Re number) which would make it usable in other flow geometries. Alternatively, it could be trained under different flow settings (e.g. different Re numbers as we do) and learn, on aggregate, the model error which in turn could be used to make predictions under different flow settings (as in our case for different Re number).

We denote with $\boldsymbol{\Sigma}$ the covariance matrix of the Gaussian likelihood which, given the absence of actual observation noise, plays the role of a tolerance parameter determining the tightness of the fit. The covariance was expressed as $\boldsymbol{\Sigma} = \text{diag}(\sigma_1^2, \dots, \sigma_{3N_{obs}}^2)$, where the values in the diagonal vector are set to 1% of the mean of the squares of each observable across the M flow settings i.e. $\sigma_i^2 = 0.01 \frac{1}{M} \sum_{m=1}^M (\hat{z}_i^{(m)})^2$.

By combining the likelihood above with the priors discussed in the previous sections as well as by employing the dimensionality reduction scheme of Equation (19) according to which $\boldsymbol{\epsilon}_\tau^{(m)}$ can be expressed as $\boldsymbol{\epsilon}_\tau^{(m)} = \mathbf{W}\mathbf{E}_\tau^{(m)}$, we obtain a posterior on:

- the parameters $\boldsymbol{\theta}$ of the parametric closure model,
- the latent variables $\mathbf{E}_\tau^{(1:M)}$ expressing the stochastic model discrepancy in *each* of the M training conditions,
- the hyperparameters $\boldsymbol{\Lambda}$ in the hyperprior of $\mathbf{E}_\tau^{(1:M)}$,

which would be of the form (omitting given hyperparameters):

$$\begin{aligned} p(\boldsymbol{\theta}, \mathbf{E}_\tau^{(1:M)}, \boldsymbol{\Lambda} | \mathcal{D}) &\propto p(\mathcal{D} | \boldsymbol{\theta}, \mathbf{E}_\tau^{(1:M)}) p(\mathbf{E}_\tau^{(1:M)} | \boldsymbol{\Lambda}) p(\boldsymbol{\theta}) p(\boldsymbol{\Lambda}) \\ &= \left(\prod_{m=1}^M p(\hat{\mathbf{z}}^{(m)} | \boldsymbol{\theta}, \mathbf{E}_\tau^{(m)}) p(\mathbf{E}_\tau^{(m)} | \boldsymbol{\Lambda}) \right) p(\boldsymbol{\theta}) p(\boldsymbol{\Lambda}). \end{aligned} \quad (23)$$

An illustration of the corresponding graphical model is contained in Fig. (1).

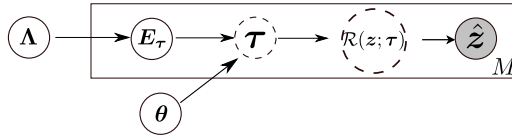


Figure 1: Probabilistic graphical model of the proposed model including model parameters ($\boldsymbol{\theta}$, $\boldsymbol{\Lambda}$), latent variables (\mathbf{E}_τ) and observables $\hat{\mathbf{z}}$ from M flow scenarios. Deterministic nodes are indicated with circles with dashed line, stochastic with circles with solid line and known/observed are shaded.

2.2.4. Inference and Learning

On the basis of the probabilistic model proposed and the posterior formulated in the previous section, we discuss numerical inference strategies for identifying the unknown parameters and latent variables. The intractability of the posterior stems from the likelihood which entails the solution of the discretized RANS equations. We advocate the use of Stochastic Variational Inference (SVI) [76] which results in a closed-form approximation of the posterior $p(\boldsymbol{\theta}, \mathbf{E}_\tau^{(1:M)}, \boldsymbol{\Lambda} | \mathcal{D})$. In contrast to the popular, sampling-based strategies (MCMC, SMC etc.), SVI yields biased estimates at the benefit of computational efficiency. Readers interested in comparative studies/discussions on SVI and MCMC in terms of accuracy and computational efficiency are directed to [77]. Given a family of probability densities $q_\xi(\boldsymbol{\theta}, \boldsymbol{\Lambda}, \mathbf{E}_\tau^{(1:M)})$ parametrized by ξ , we find the optimal, i.e. the one that is closest to the exact posterior in terms of their Kullback-Leibler divergence, by maximizing the Evidence Lower Bound (ELBO) $\mathcal{F}(\xi)$ [68]:

$$\begin{aligned} \mathcal{F}(\xi) &= \mathbb{E}_{q_\xi(\boldsymbol{\theta}, \boldsymbol{\Lambda}, \mathbf{E}_\tau^{(1:M)})} \left[\log \left(\frac{p(\mathcal{D}, \boldsymbol{\theta}, \boldsymbol{\Lambda}, \mathbf{E}_\tau^{(1:M)})}{q_\xi(\boldsymbol{\theta}, \boldsymbol{\Lambda}, \mathbf{E}_\tau^{(1:M)})} \right) \right] \\ &= \mathbb{E}_{q_\xi(\boldsymbol{\theta}, \boldsymbol{\Lambda}, \mathbf{E}_\tau^{(1:M)})} \left[\log \left(\frac{p(\mathcal{D} | \boldsymbol{\theta}, \mathbf{E}_\tau^{(1:M)}) p(\mathbf{E}_\tau^{(1:M)} | \boldsymbol{\Lambda}) p(\boldsymbol{\theta}) p(\boldsymbol{\Lambda})}{q_\xi(\boldsymbol{\theta}, \boldsymbol{\Lambda}, \mathbf{E}_\tau^{(1:M)})} \right) \right]. \end{aligned} \quad (24)$$

As its name suggests, it can be readily shown and that ELBO lower-bounds the model log-evidence and their difference is given by the aforementioned KL-divergence i.e.:

$$\log p(\mathcal{D}) = \mathcal{F}(\xi) + KL(q_\xi(\boldsymbol{\theta}, \boldsymbol{\Lambda}, \mathbf{E}_\tau^{(1:M)}) || p(\boldsymbol{\theta}, \boldsymbol{\Lambda}, \mathbf{E}_\tau^{(1:M)} | \mathcal{D})). \quad (25)$$

In order to expedite computations we employ a mean-field assumption [77] according to which the approximate posterior is factorized as:

$$q_\xi(\boldsymbol{\theta}, \boldsymbol{\Lambda}, \mathbf{E}_\tau^{(1:M)}) = q_\xi(\boldsymbol{\theta}) q_\xi(\boldsymbol{\Lambda}) \prod_{m=1}^M q_\xi(\mathbf{E}_\tau^{(m)}). \quad (26)$$

We employ Dirac-deltas for the first two densities i.e.:

$$q_\xi(\boldsymbol{\theta}) = \delta(\boldsymbol{\theta} - \boldsymbol{\theta}_{MAP}), \quad (27)$$

$$q_\xi(\boldsymbol{\Lambda}) = \delta(\boldsymbol{\Lambda} - \boldsymbol{\Lambda}_{MAP}). \quad (28)$$

In essence, we obtain point estimates for $\boldsymbol{\theta}, \boldsymbol{\Lambda}$ which coincide with the Maximum-A-Posteriori (MAP) estimates. The specific choice of Dirac-deltas was motivated by computational cost reasons in the inference and prediction steps. Furthermore, given that the dimension of $\boldsymbol{\theta}$ is generally (much) smaller than the number of observations (see section 3), we anticipate that its posterior would not deviate much from a Dirac-delta. The final reason for which posterior uncertainty (albeit small) on $\boldsymbol{\theta}$ was not included, was to emphasize the significance and impact of the stochastic, model correction term that we propose.

For the model discrepancy variables $\mathbf{E}_\tau^{(m)}$, we employ uncorrelated Gaussians given by:

$$q_\xi(\mathbf{E}_\tau^{(m)}) = \mathcal{N}(\mathbf{E}_\tau^{(m)} | \boldsymbol{\mu}_E^{(m)}, \text{diag}(\boldsymbol{\sigma}_E^{2,(m)})), \quad \forall i \in \{1, \dots, M\}. \quad (29)$$

In summary, the vector ξ of the parameters in the variational approximation consists of:

$$\xi = \{\theta_{MAP}, \Lambda_{MAP}, \{\mu_E^{(m)}, \sigma_E^{2,(m)}\}_{m=1}^M\}. \quad (30)$$

The updates of the parameters ξ are carried out using derivatives of the ELBO. These entail expectations with respect to q_ξ which are estimated (with noise) by Monte Carlo in conjunction with the ADAM stochastic optimization scheme [78]. In order to reduce the Monte-Carlo noise in the estimates, we employ the reparametrization trick [79]. This is made possible here due to the form of the approximate posterior q_ξ . In particular, if we summararily denote with $\eta = \{\theta, \Lambda, \mathbf{E}_\tau^{(1:M)}\}$ and given that the approximate posterior $q_\xi(\eta)$ can be represented by deterministic transform $\eta = g_\xi(\phi)$, where ϕ follows a known density $q(\phi)^2$, the expectations involved in the ELBO and, more importantly, in its gradient can be rewritten as:

$$\nabla_\xi \mathcal{F}(\xi) = \mathbb{E}_{q(\phi)} \left[\nabla_\xi g_\xi(\phi) \nabla_\eta \left(\log p(\mathcal{D}, \eta) - \log q_\xi(\eta) \right) \right]. \quad (31)$$

One observes that derivatives of the log-likelihood with respect to η are needed. This in turn would imply derivatives of the RANS-model outputs with respect to $\{\theta, \Lambda, \mathbf{E}_\tau^{(1:M)}\}$ which appear indirectly through τ . Such derivatives are rendered possible by using an adjoint formulation of the discretized RANS model that yields in effect a *differentiable* solver.

Further details about the derivatives of the ELBO and the use of RANS-model sensitivities obtained by an adjoint formulation can be found in Appendix B. An algorithmic summary of the steps entailed is contained in Algorithm 1. We note finally that the ELBO \mathcal{F} (which serves as a lower bound to the model evidence) and can be used to compare (in a Bayesian sense) alternative models. Such model variations could arise by changing e.g. \mathbf{W} i.e. the partition into subdomains which enables the dimensionality reduction of the stochastic model discrepancy vector. One could even employ an adaptive division into subdomains guided by \mathcal{F} so as the data can dictate which regions require more/less refinement.

2.2.5. Predictions

In this section, we describe how *probabilistic*, predictive estimates of any quantity of interest related to the RANS-simulated flow can be produced using the trained model. In particular, one can obtain a *predictive, posterior density* $p(z|\mathcal{D})$ on the whole solution vector z of the RANS equations as follows:

$$\begin{aligned} p(z|\mathcal{D}) &= \int p(z, \mathbf{E}_\tau, \theta, \Lambda | \mathcal{D}) d\mathbf{E}_\tau d\theta d\Lambda \\ &= \int p(z | \mathbf{E}_\tau, \theta) p(\mathbf{E}_\tau, \theta, \Lambda | \mathcal{D}) d\mathbf{E}_\tau d\theta d\Lambda \\ &= \int p(z | \mathbf{E}_\tau, \theta) p(\mathbf{E}_\tau | \Lambda) p(\theta, \Lambda | \mathcal{D}) d\mathbf{E}_\tau d\theta d\Lambda. \end{aligned} \quad (32)$$

The third of the densities in the integrand is the posterior which is substituted by its variational approximation i.e. q_ξ in Equation (26) and for the optimal parameter values ξ identified as described in the previous section. The second of the densities represents the prior model prescribed in Equation (20). Finally, the first of the densities is simply a Dirac-delta which corresponds to the solution of the RANS equations obtained when using the proposed closure model for given

²Based on the form of q_ξ in Equations (26),(27), (28), (29), the transform employed can be written as $\theta = \theta_{MAP}$, $\Lambda = \Lambda_{MAP}$ and $\mathbf{E}_\tau^{(m)} = \mu_E^{(m)} + \text{diag}(\sigma_E^{2,(m)}) \phi$ where $q(\phi) = \mathcal{N}(\phi | \mathbf{0}, \mathbf{I})$.

Algorithm 1: Inference and Learning using SVI

Input : $\mathcal{D} = \{\hat{z}^{(i)}\}_{i=1}^M, \mathbf{W}$
Output: $\xi = \{\theta_{MAP}, \Lambda_{MAP}, \{\mu_E^{(m)}, \sigma_E^{2,(m)}\}_{m=1}^M\}$

- 1 **while** $ELBO \hat{\mathcal{F}}$ not converged **do**
- 2 $\theta \leftarrow \theta_{MAP}, \Lambda \leftarrow \Lambda_{MAP};$
- 3 **for** $m \in \{1 : M\}$ **do**
- 4 **for** $k \in \{1 : K\}$ **do**
- 5 // Reparametrization trick
 Sample $\phi^{(m,k)} \sim \mathcal{N}(\mathbf{0}, \mathbf{I})$ for $k = 1, \dots, K$;
- 6 // Compute stochastic discrepancy terms
 $\mathbf{E}_\tau^{(m,k)} = g_\xi(\phi^{(m,k)}) = \mu_E^{(m)} + \sigma_E^{(m)} \odot \phi^{(m,k)}$;
- 7 // Solve discretized RANS equations
 Solve $\mathcal{R}(z; \tau_\theta(\mathbf{u}) + \mathbf{W}\mathbf{E}_\tau^{(m,k)}) = 0$ to obtain the solution vector $\mathbf{z}^{(m,k)}$;
 // Equation (12)
- 8 // Compute log-likelihoods and their gradients
 $\ell^{(m,k)}(\theta, \mathbf{E}_\tau^{(m,k)}), \partial \ell^{(m,k)} / \partial \theta, \partial \ell^{(m,k)} / \partial \mathbf{E}_\tau^{(m,k)}$; // Equations (B.3),
 (B.8), (B.9)
- 9 **end**
- 10 **end**
 // Monte Carlo estimate of ELBO
- 11 Estimate ELBO \mathcal{F} using Equation (B.10);
 // Monte Carlo estimate of the gradient of the ELBO
- 12 Estimate gradient of ELBO $\nabla_\xi \mathcal{F}$ using Equation (B.12);
 // Stochastic Gradient Ascent
- 13 $\xi^{(n+1)} \leftarrow \xi^{(n)} + \rho^{(n)} \odot \nabla_\xi \mathcal{F}$;
- 14 $n \leftarrow n + 1$;
- 15 **end**
- 16 **return** ξ

\mathbf{E}_τ, θ . Since the RANS solver is a black-box, it would not be possible to propagate the uncertainty in \mathbf{E}_τ (and potentially θ) otherwise. In practical terms and given the intractability of this integral, the equation above suggests a Monte Carlo scheme for obtaining samples from $p(\mathbf{z}|\mathcal{D})$ which involves the following steps. For each sample:

- Set $\theta = \theta_{MAP}, \Lambda = \Lambda_{MAP}$. (If a different variational approximation to the posterior q_ξ than the one in Equations (27), (28) were used, then θ, Λ would need to be sampled from it).
- Sample \mathbf{E}_τ from $p(\mathbf{E}_\tau|\Lambda_{MAP})$ in Equation (20) and compute model discrepancy vector $\epsilon_\tau = \mathbf{W}\mathbf{E}_\tau$.
- Solve the discretized RANS model in Equation (12) for $\tau = \tau_\theta(\mathbf{u}) + \epsilon_\tau$.

Other numerical integration techniques (e.g. Quasi Monte Carlo or Importance Sampling) could be used in order to obtain estimates of the integral with fewer RANS solves. The aforementioned

steps would need to be repeated for as many samples as desired. Subsequently, the samples can be used to compute statistics of the predictive estimate (e.g. predictive mean, variance, credible intervals, etc) not only of \mathbf{z} (i.e. velocities/pressures) but of any quantity of interest such as the lift, drag, skin friction, etc.

We note however that stochastic RS discrepancy terms ϵ_τ or \mathbf{E}_τ and the associated probabilistic model, are limited to the flow geometry used for the training. While it can be used for unseen flow scenarios (e.g. different Re number, inlet conditions, boundary conditions), it cannot be employed for a different flow geometry. In theory, the parametrization of the ϵ_τ can be updated to accommodate different geometries, but we leave it for future investigations. Finally, we would like to highlight the fact that baseline RANS data *is not needed* as an input to the neural networks for prediction in the proposed scheme, as opposed to other frameworks that have been employed in the past (e.g. [22, 15, 17, 65]).

In terms of computational aspects, the stochastic nature of the (reduced) discrepancy tensor \mathbf{E}_τ can potentially introduce non-smoothness in the RS vector $\boldsymbol{\tau}$ used for solving the RANS equations. In the present work, we have used diagonal covariance for the hyper-prior of \mathbf{E}_τ given by $\boldsymbol{\Lambda} = \text{diag}(\boldsymbol{\Lambda}^{(J)})$, $J = 1, \dots, N_d$, thus assuming there is no correlation among the nearby nodes/region. As an avenue for future work, a banded covariance matrix can be employed to capture such spatial correlations. Sparsity-inducing priors that account for spatial correlations have been proposed in [80, 73]. A schematic overview of the methodological framework discussed in Section (2.2.4) and Section (2.2.5) is presented in Fig. (2). Numerical results, training data and the corresponding source code will be made available at <https://github.com/pkmtum/D3C-UQ> upon publication.

3. Numerical Illustrations

3.1. Test case: Backward Facing step

We select the backward facing step configuration in order to assess the proposed modeling framework. This is a classic benchmark problem that has been widely used for studying the performance of turbulence models as it poses significant challenges due to the complex flow features such as flow separation, reattachment and recirculation [81, 82]. In this setup, as illustrated in Fig. (3) a two-dimensional channel flow is abruptly expanded into a rectangular cavity with a step change in height. The flow separates at the step and forms two recirculation zones downstream, one directly after the step and the other on the upper channel wall downstream. These two recirculation zones affect the reattachment length. The flow features can be seen in more detail as depicted in the LES simulations in Fig. (6). In this setting, the Reynolds number is defined as:

$$Re = \frac{uh}{\nu}, \quad (33)$$

where h and ν are the characteristic length (also the step height) and kinematic viscosity, respectively and u denotes the average velocity of the inlet flow. In the present study, the expansion ratio H/h is 2 and the boundary conditions are shown in Fig. (3). They consist of constant inlet bulk velocity $u_b = 1$ in the x -direction ($u_b = u$) on the left boundary, no-slip condition on Γ_D (i.e, top/bottom boundary) and zero tractions along Γ_N (i.e, at the outflow boundary) i.e. $(-p\mathbf{I} + \frac{\nu}{2}(\nabla\mathbf{u} + \nabla\mathbf{u}^T)) \cdot \hat{\mathbf{n}} = 0$ where $\hat{\mathbf{n}}$ is the outward normal of the outflow. On the $x - y$ plane, we place the origin at the corner of the step.

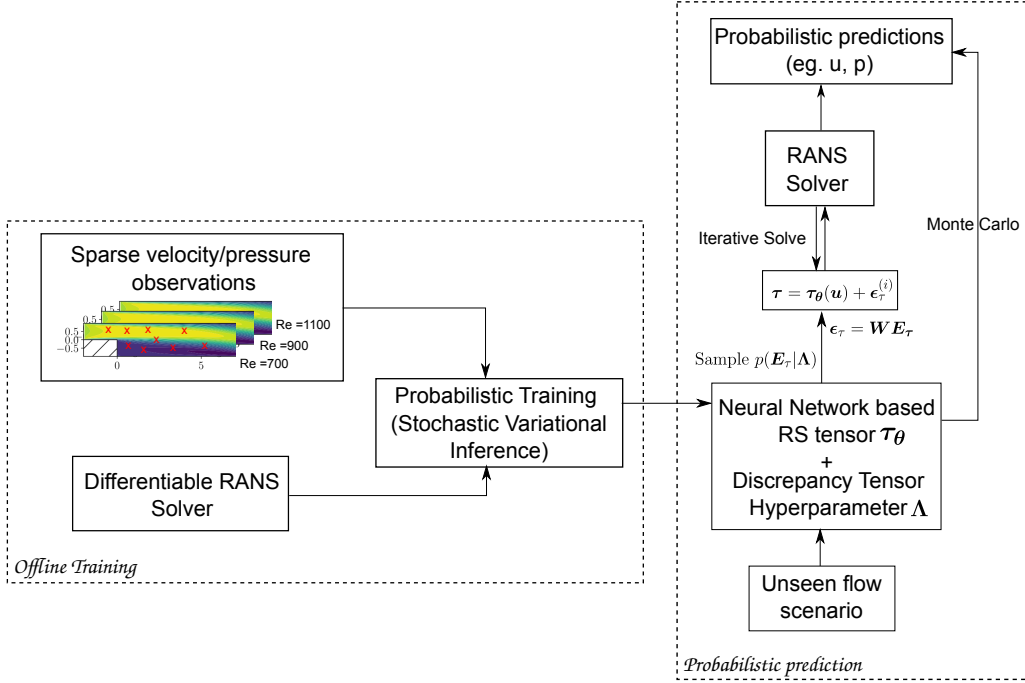


Figure 2: Schematic illustration of the training/inference (left block) and probabilistic prediction (right block) framework proposed.

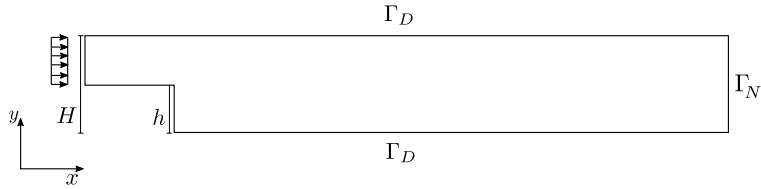


Figure 3: Backward facing step flow configuration with step height h and the total channel height H . The origin of the $x - y$ plane is placed at the corner of the step. The axes are depicted at the bottom left to avoid clutter.

3.2. Generation of training data

In order to generate the training data, we performed Large Eddy Simulations (LES) for various Reynolds numbers i.e. by varying the kinematic viscosity ν . A three-dimensional configuration is adopted wherein the z -direction (i.e. the in-plane direction) is periodic and the mean fields averaged over the z -direction are used for training. We also performed RANS simulations using the $k - \epsilon$ model for the same set of Re numbers to provide a comparison as it is the most widely used RANS model in industrial applications. In the subsequent discussions, we will refer to the $k - \epsilon$ model as the **baseline RANS model**.

We used the open-source CFD platform OpenFOAM [83] for the LES and baseline RANS simulations. We utilized the steady-state, incompressible solver simpleFoam for the baseline RANS simulations. This solver uses the Semi-Implicit Method for Pressure Linked Equations (SIMPLE) in order to solve both the momentum and pressure equations. For the LES simulations,

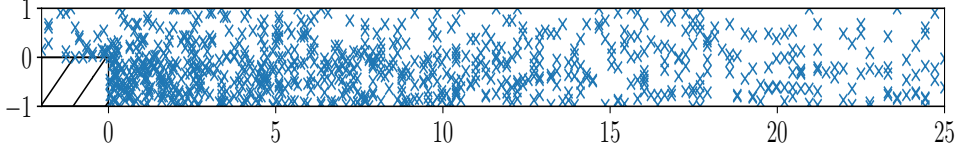


Figure 4: (Random) grid points where LES velocities/pressure were used for training data. We note that the total number of LES grid points is $O(10^5)$ whereas LES simulation data at approximately 1000 grid points were employed.

we employed the pimpleFoam transient solver, which combines both the PISO (Pressure Implicit with Split Operator) and SIMPLE algorithms to solve the pressure and momentum equations. In particular, we use the WALE (Wall-Adapting Local Eddy-Viscosity) model [84]. This model is well-suited for capturing turbulent structures near solid walls and is known for its accurate predictions of wall-bounded turbulent flows. In order to overcome the computational demands of LES, a domain decomposition approach was employed. In particular, we split the domain into 16 subdomains and leverage the CPU cores in parallel³. We discretized both the baseline RANS and LES domains using second-order methods and all the meshes were non-uniform with mesh density increasing in the domains of interest. To ensure numerical accuracy, we ran all simulations with a CFL number below 0.3. Other pertinent details of the LES and baseline simulations are provided in Table 2. We note that the purpose of the LES model in the present work is to serve as the reference solver that the trained RANS model would try to approximate or match. The framework proposed does not make use of the particulars of the LES solver and one could readily use actual or DNS data (or combinations thereof) for training. The LES data might deviate from physical reality or the results obtained by DNS. Readers interested in the relative accuracy of LES simulations are directed to [85, 86].

The mean field reference data from LES is interpolated to the same mesh used for the Finite Element (FE)-based calibrated RANS model (model implementation details discussed in the sequel). However, not all the observations in the grid were used for training. At each RANS grid point, an independent, random coin was flipped with probability 10% of picking the grid point. This resulted in **mean velocity/pressure observations at approximately 8% of the grid points to be used as training data**, i.e. a rather sparse dataset (the selected observation points are depicted in Fig. (4)). Naturally, the density of RANS grid was higher near the step, so the density of observations was higher in the regions of steeper velocity gradients (in the reattachment and recirculation regions) and lower in other regions. Hence, the training dataset $\mathcal{D} = \{\hat{\mathbf{z}}^{(i)}\}_{m=1}^M$ consists of the velocities/pressure at those grid points obtained from the $M = 4$ LES simulations carried out with the corresponding Re numbers (in Table 2). . The influence of the number of observation points on the learning and predictive results is an interesting research direction, which we will address in future investigations. A few snapshots of the instantaneous velocity magnitude for $Re = 1100$ from the LES simulation are depicted in Fig. (5) where one can observe how the flow features of interest evolve over time. Only the time-averaged velocities/pressures were used for training which are shown in Fig. (6).

³Computations were carried out in a Intel Core i9-12900K CPU.

Domain Size	$27h \times 2h \times h$
DoF LES	1428920
DoF $k - \epsilon$	35709
step height (h)	1
Total channel height (H)	2
kinematic viscosity ν values for training data generation ($\times 10^{-3}$)	3.33, 2.00, 1.42, 1.11, 0.909
Re values for training data generation	300, 700, 900, 1100
Re value for prediction	500
characteristic length	step height h

Table 2: Parameters used for performing the CFD simulations for the generation of the training and test data [51]

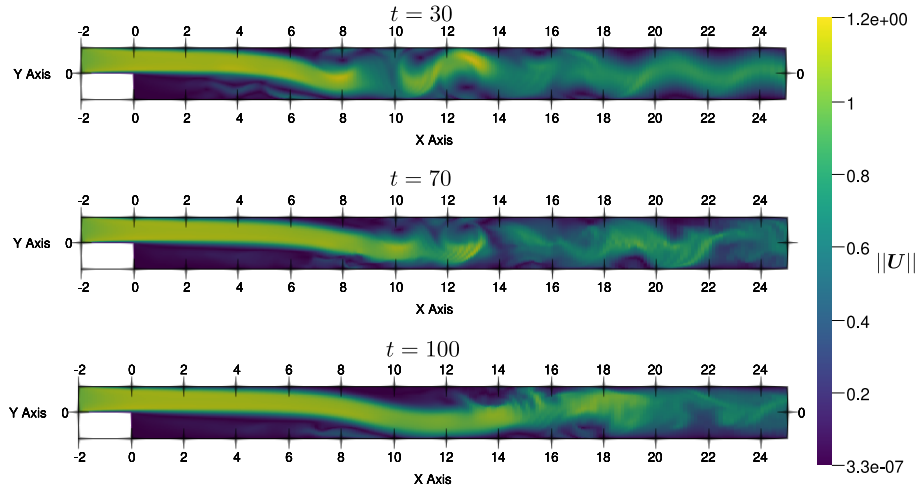


Figure 5: Instantaneous velocity magnitude $\|U\|$ at different time-instants $t = \{30, 70, 100\}$ obtained from the LES simulation performed at $Re = 1100$. We note that the flow eventually reaches a stationary state.

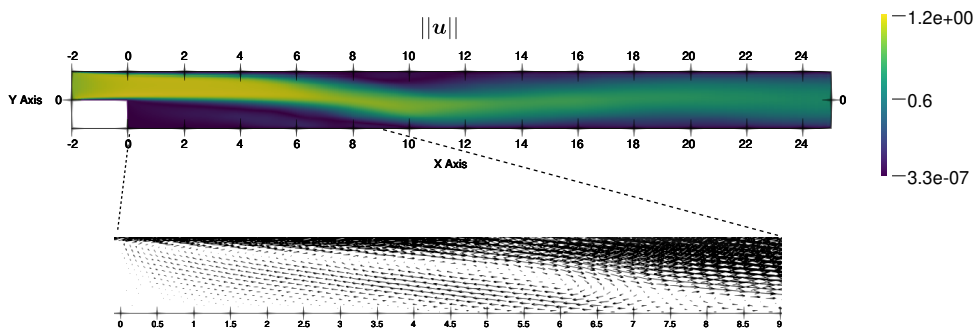


Figure 6: Time-averaged velocity magnitude $\|u\|$ obtained from LES simulation performed at $Re = 1100$. The velocity vector plot highlights the flow separation, recirculation zones and the flow reattachment.

3.3. Differentiable forward RANS solver and probabilistic learning implementation

For the discretization of the RANS equations (Equation (12)) the Finite Element (FE) method was employed and the implementation was carried out in the open source package `FEniCS` [87] due to its innate adjoint solver [88]. The basic quantities and their dimensions are listed in Table 3. Further details about the differentiable solver can be found in Appendix A.

Probabilistic inference and learning tasks were performed using the probabilistic programming package `Pyro` [89] which is built on top of the popular machine learning library `PyTorch` [90]. The ELBO maximization was performed using the ADAM scheme [78]. The number of Monte Carlo samples used at each iteration for the estimation of the ELBO and its gradient was $K = 5$ (Algorithm 1). The gradient computation of the ELBO (Equation (31)) was enabled by overloading the `autograd` functionality of PyTorch to facilitate interaction between the solver’s adjoint formulation and the auto-differentiation-based neural network gradient. A relatively small learning rate of 10^{-6} was employed due to the Monte Carlo noise in the ELBO gradients. The neural network architecture employed for the parametric RS model was identical to the one suggested by [15] where the optimal number of hidden layers and nodes per layer was determined to be 8 and 30 respectively. The Leaky ReLU was chosen as the activation function for all layers. We noted however that the usual practice of random weight initialization was unsuitable as it led to divergence of the solution even after applying the stabilization schemes. For this reason, we used baseline RANS closure data with added noise to pre-train the neural network in order to provide a suitable initialization.

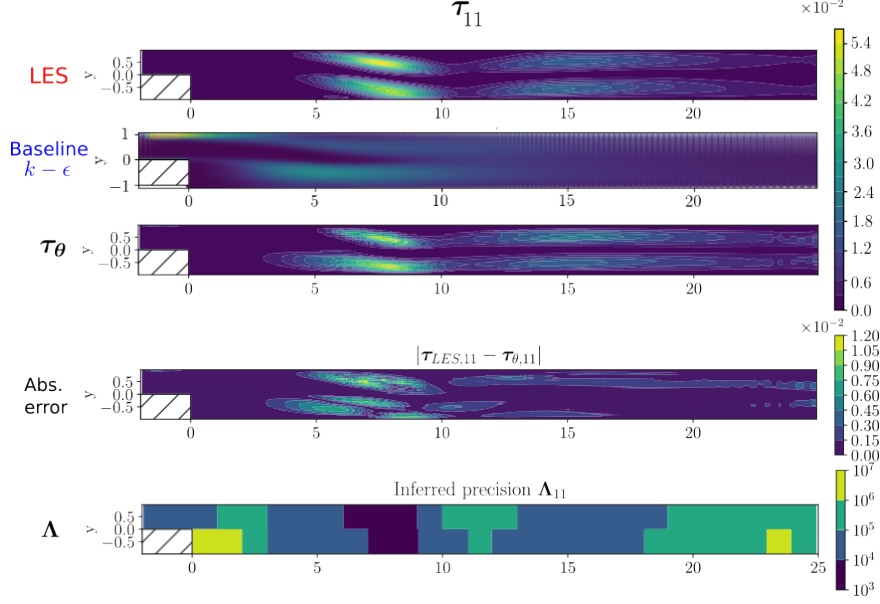
Quantity	dimensions
Domain Size	$27h \times 2h$
number of nodes in FE simulation (N)	12180
$\dim(\mathbf{z})$	12180×3
$\dim(\boldsymbol{\tau})$	12180×3
Boolean Matrix $\dim(\mathbf{W})$	12180×52
$\dim(\mathbf{E})$	52×3
$\dim(\boldsymbol{\Lambda})$	52×3
$\dim(\boldsymbol{\theta})$	6970

Table 3: Basic quantities and dimensions

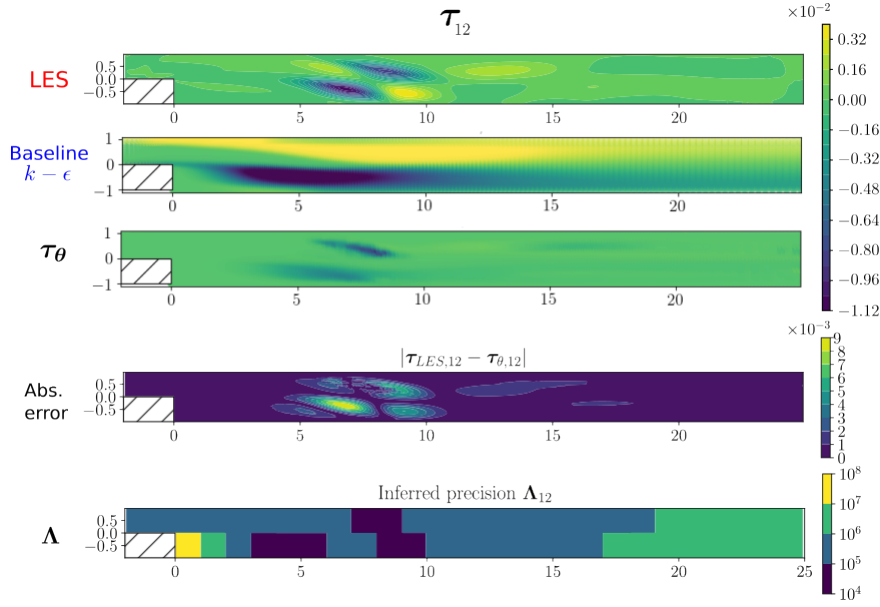
3.4. Results and Discussion

We assessed the trained model for the test-case with $Re = 500$ which was not contained in the training data. In the sequel, various aspects of the probabilistic predictions obtained as described in Section (2.2.5) are compared with the reference LES and the baseline RANS predictions. Even though the same *parametrized* RS closure term was used in [15] (and other subsequent works branching from this), their results are not directly comparable due to the use of blending functions [17, 22], which combine baseline RS values near the walls with the constant, predicted RS in the bulk and with the amount of blending being case-dependent.

The performance of the proposed method in predicting the components of the RS tensor is shown in Fig. (7), from which the following conclusions can be drawn:

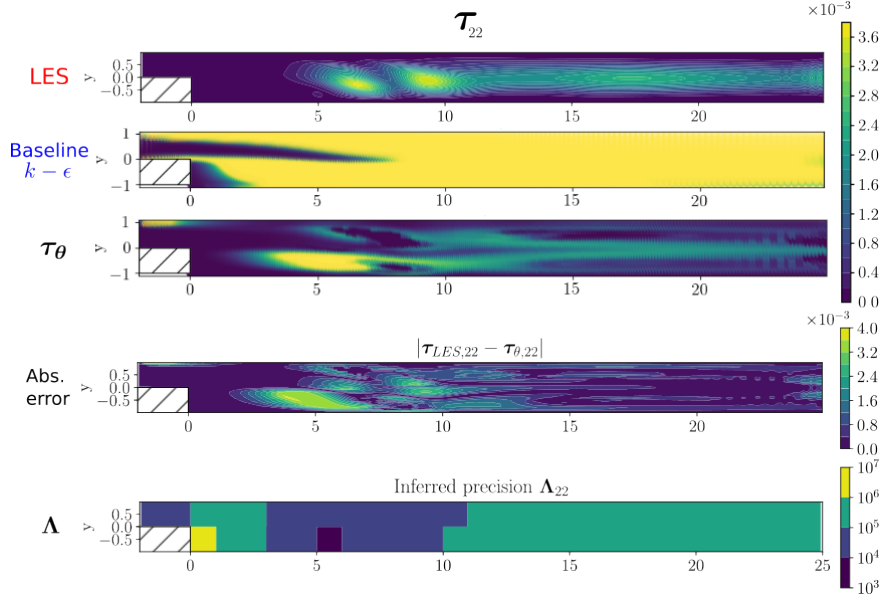


(a) Comparison for τ_{11} .



(b) Comparison for τ_{12} .

Figure 7: Comparison of the predicted components of the RS tensor τ_θ with the LES reference values and the *baseline* RANS ($k - \epsilon$) for the test case with $Re = 500$. The three components τ_{11} , τ_{12} and τ_{22} are separately compared in subfigures (a), (b), and (c) respectively (*subfigure (c) in the next page*). In each block, **top** - the LES RS tensor component contour, **second** - the $k - \epsilon$ RS tensor component contour, **third** - the predicted, parametric RS tensor τ_θ for $\theta = \theta_{MAP}$, **fourth** - the contour plot of the absolute error between the LES RS tensor and the τ_θ tensor component, **bottom** - the inferred hyper-parameter Λ of the (reduced) discrepancy tensor E_τ .



(c) Comparison for τ_{22} .

Figure 7: (cont. from the previous page) Comparison of the predicted components of the RS tensor τ_θ with the LES reference values and the *baseline* RANS ($k - \epsilon$) for the test case with $Re = 500$. The three components τ_{11} , τ_{12} and τ_{22} are separately compared in subfigures (a), (b) and (c) respectively (*subfigure (a) and (b) in the next page*). In each block, **top** - the LES RS tensor component contour, **second** - the $k - \epsilon$ RS tensor component contour, **third** - the predicted, parametric RS tensor τ_θ for $\theta = \theta_{MAP}$, **fourth** - the contour plot of the absolute error between the LES RS tensor and the τ_θ tensor component, **bottom** - the inferred hyper-parameter Λ of the (reduced) discrepancy tensor E_τ .

- Even though **no RS observations** were provided during the training, the parametric τ_θ (i.e. neural-network based) part of the RS closure is able to capture the basic features of the reference (i.e. LES) RS field. In contrast, the baseline $k - \epsilon$ model severely under/over-estimates its magnitude and misrepresents its spatial variability. We observe that some regions have relatively higher errors (for e.g., around $5 < x/h < 10$ in Fig. (7c)), which is attributed to the parametric model's inability to provide adequate closure. This model error is exactly what we attempt to capture with our proposed stochastic discrepancy term.
- The bottom row of all the three subfigures in Fig. (7) depicts the inferred precision Λ of the (reduced) discrepancy tensor E_τ . As this is inversely proportional to the predictive uncertainty we note that it attains smaller values in the regions where the parametric model τ_θ deviates the most from the LES values (e.g. for $5 < x/h < 10$). Conversely, it attains very large values (which correspond to practically zero model discrepancies) in areas where the parametric closure model is able to correctly account for the underlying phenomena (e.g. far downstream and for all three RS components). This is expected as the flow attains an almost parabolic profile in this region, which in turn translates to reduced fluctuations in the RS tensor, making it easier for the neural network to learn.

The Monte-Carlo-based scheme (detailed in Section (2.2.5)) was employed to propagate the model form uncertainty forward in order to obtain probabilistic predictive estimates for the quantities of interest i.e. mean stream-wise velocity u , wall-normal velocity v (Fig. (8), Fig. (9)) and

mean pressure p (Fig. (10)). Cross-sections of the aforementioned quantities are depicted in Fig. (11). The following conclusions can be drawn from the Figures:

- Even though the RS field is captured with some discrepancies, the predicted mean fields agree well with the reference LES data (Figures 8, 9 and 10, discussed in the sequel). This points to the non-uniqueness of this inverse problem solution, also reported by other works [7, 37].
- There exist two recirculation zones in the backward-facing step flow setup. The primary one forms just after the step and the secondary appears above it for Reynolds numbers close to 400 and above, for the given expansion ratio [91]. As it can be seen in Fig. (8), the proposed model is able to predict the appearance of the two recirculation zones in close agreement with the LES, whereas the baseline RANS model underestimates the size of the first recirculation zone and almost completely misses the second one.
- The last row of Fig. (8) depicts the predictive posterior standard deviation of the aforementioned quantities. As expected, around the shear layers (the top of the first recirculation zone and the bottom of the second recirculation zone), the uncertainty is the highest. This is even more clearly observed in the cross-sections of Fig. (11) which illustrate the predictive, posterior mean plus/minus two posterior standard deviations. More importantly perhaps, one observes that the predictions envelop the reference LES values in most areas. The model is extremely confident close to the inlet, as manifested by the very tight credible interval. As one moves further downstream and close to the first recirculation zone, the parametric closure suffers, hence the uncertainty bounds are wider to account for it. The ability to quantify aleatoric, predictive uncertainty⁴ is one of the main advantages of the probabilistic model proposed in contrast to the more commonly used deterministic counterparts as well as alternatives that can only capture epistemic uncertainty.
- Similarly to the stream-wise velocity, predictions for the wall-normal velocity (Fig. (9)) and the pressure (Fig. (10)) are in good agreement with the reference LES values, as opposed to the baseline RANS. In the first recirculation zone, the baseline $k - \epsilon$ is completely off, while the predicted values with the credible interval cover the reference LES. Also, the pressure predictions (Fig. (10)) identify the crucial zone where the flow reattaches to the wall (around $x/h \approx 10$), which is very difficult to predict in general. At the reattachment point, there is a transition from low-pressure in the recirculation zone to higher pressure along the wall. The posterior standard deviation at this point is also higher than in the other regions, ensuring that the reference solution is enveloped.

As previously mentioned, observations of mean velocities/pressures at approximately 8% of the total number of grid points in the FE mesh were used for training. Fig. (12) highlights this by comparing the stream-wise velocity at three different sections x/h . The left subfigure depicts the section in the first re-circulation zone. It can be seen that despite having very few observation points near the wall, the u predictions are able to capture the backward flow in the re-circulation regions. In contrast, the baseline $k - \epsilon$ completely fails to capture it. This can be attributed to the earlier reattachment of the flow in the baseline $k - \epsilon$ case (flow reattachment discussed in the sequel). The middle and the right subfigures depict sections further downstream, with the middle

⁴As mentioned earlier, MAP point-estimates for the model parameters θ were used.

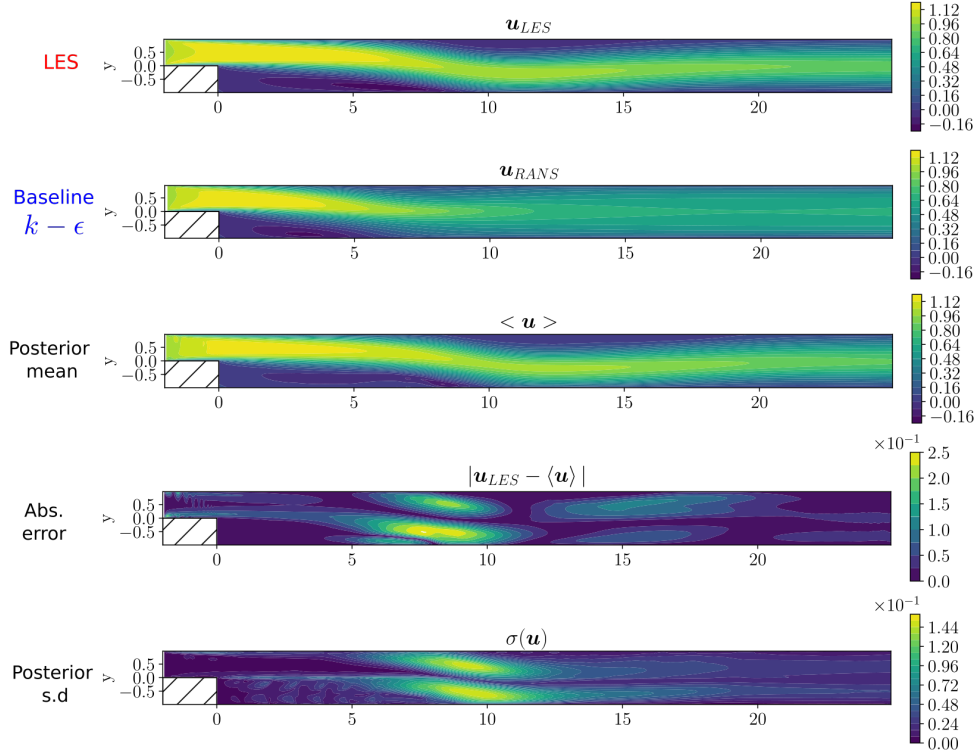


Figure 8: Velocity contours in x-direction (\mathbf{u}) for the test case with $Re = 500$. **top** - ground truth (LES), **second** - baseline $k - \epsilon$, **third** - the posterior predictive mean ($\langle \mathbf{u} \rangle$), **fourth** - the contour plot of the absolute error between the LES (\mathbf{u}_{LES}) and the posterior predictive mean ($\langle \mathbf{u} \rangle$), **bottom** - the standard deviation of the posterior predictive ($\sigma(\mathbf{u})$).

being in the second re-circulation zone and the right in the flow recovery zone. It is observed that with a relatively small number of observation points, the trained model's prediction is in agreement with the LES. Furthermore, the latter is enveloped by the credible interval constructed by considering $\pm 3 \times$ (the posterior standard deviation). This credible interval is much tighter as compared to the one in the left subfigure.

The primary motivation behind RANS models and of this work is to reduce the computational cost of flow simulations, especially in cases where LES or DNS are prohibitively expensive. In Table 4 we report the computational time of a single, model run as compared to the baseline RANS model (for $Re = 500$). We observe that even though the proposed differentiable solver is of comparable cost to the baseline RANS, it can provide far more accurate, probabilistic predictions of the LES model's outputs which is roughly 6000 times more computationally demanding.

Accurately capturing the recirculation zones is crucial to getting a reliable estimate of the reattachment length, which is a key parameter in the study of separated flows, such as the case here. The reattachment length is defined as the distance from the step where the flow separates to the point at which it reattaches to the surface downstream of the step. Reattachment occurs where the velocity gradient off the wall is zero, or in other words, where the wall shear stress is zero. The predicted reattachment length ($x_{reattach}$) by the proposed method is compared with a) the LES data (Section (3.2)) b) the baseline RANS (Section (3.2)) c) the two-dimensional, LES

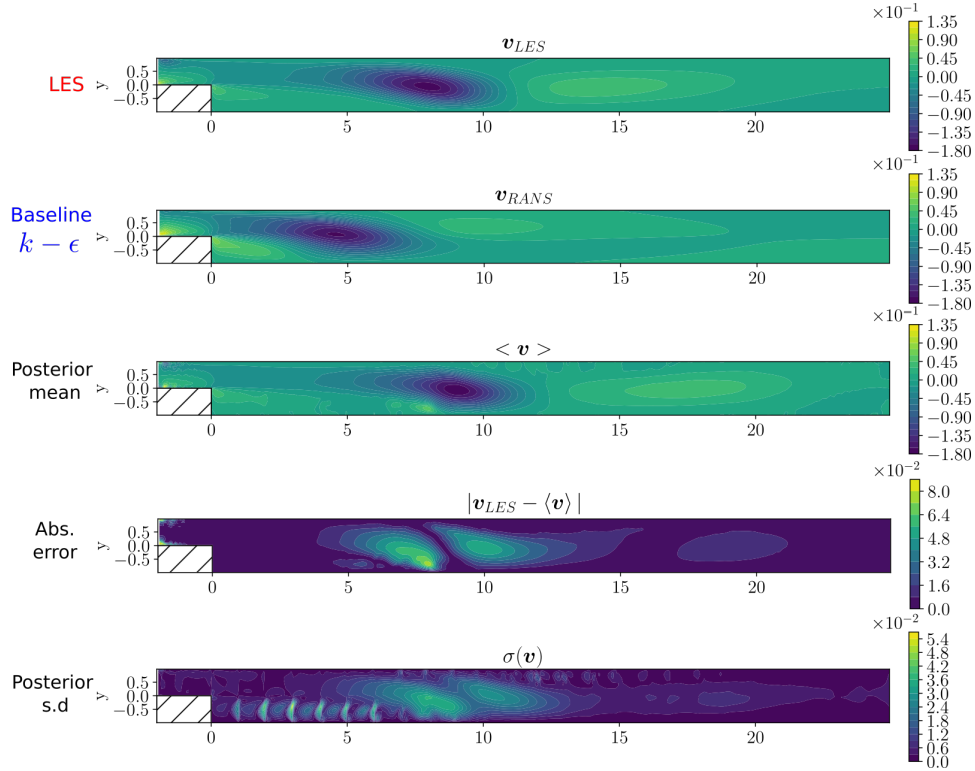


Figure 9: Velocity contours in y -direction (v) for the test case with $Re = 500$. **top** - ground truth (LES), **second** - baseline $k - \epsilon$, **third** - the posterior predictive mean ($\langle v \rangle$), **fourth** - the contour plot of the absolute error between the LES (v_{LES}) and the posterior predictive mean ($\langle v \rangle$), **bottom** - the standard deviation of the posterior predictive ($\sigma(v)$).

	LES	proposed RANS solver
Relative cost	7679	1.3

Table 4: Relative computational cost in terms of computational time (on an Intel Core i9-12900K CPU) of a single model run for LES and of the proposed, differentiable RANS solver. These are compared with the cost of the baseline RANS model for Reynolds number 500.

simulation performed by [92] for the expansion ratio of 1.9423, and d) the results in [22], who used the same Tensor Basis Neural Networks (TBNN) [15] employed in the parametric closure term in our work as well. The results are summarized in Table 5 where it is evident that while previous works deviated significantly from the reference LES value, our probabilistic prediction is able to envelop it. The reattachment length is heavily dependent on correctly identifying the two recirculation zones and the baseline RANS model fails to predict the secondary recirculation zone (Fig. (8)). This might have resulted in such a low reattachment length. The estimate of the reattachment length is also low in [22], which could be attributed to the lack of the stochastic, model correction term.

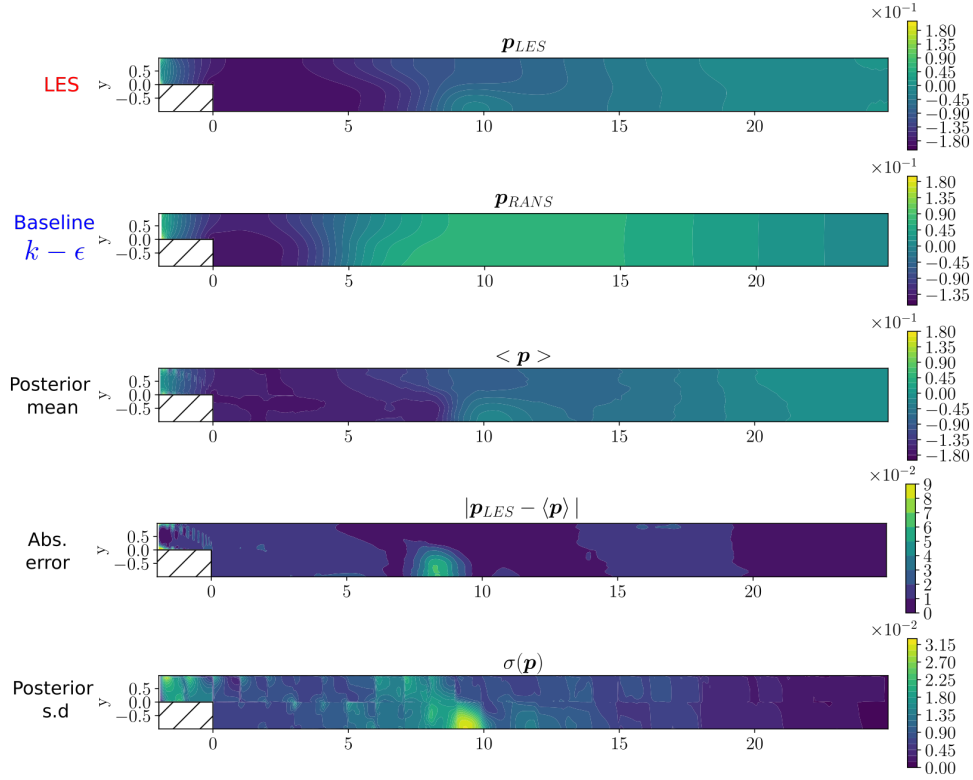


Figure 10: Pressure contours (p) for the test case with $Re = 500$. **top** - ground truth (LES), **second** - baseline $k - \epsilon$, **third** - the posterior predictive mean ($\langle u \rangle$), **fourth** - the contour plot of the absolute error between the LES (p_{LES}) and the posterior predictive mean ($\langle p \rangle$), **bottom** - the standard deviation of the posterior predictive ($\sigma(u)$).

Model	$x_{reattach}[x/h]$
LES (reference)	9.10
Biswas et al. [92] ($H/h = 1.9423$)	8.9
Baseline RANS ($k - \epsilon$ model)	5.61
Geneva et al.[22]	5.52
proposed model	10.06 ± 1.21

Table 5: Predictions of reattachment length (x/h) of the primary recirculation region behind the backward-facing step (expansion ratio $H/h = 2$) for the test case with $Re = 500$. The \pm corresponds to $3 \times$ the posterior standard deviation.

4. Conclusions

We have presented a data-driven model for RANS simulations that quantifies and propagates in its predictions an often neglected source of uncertainty, namely the aleatoric, model uncertainty in the closure equations. We have combined this with a parametric closure model which employs a set of tensor basis functions that depend on the invariants of the rate of strain and rotation tensors. A fully Bayesian formulation is advocated which makes use of a sparsity-inducing

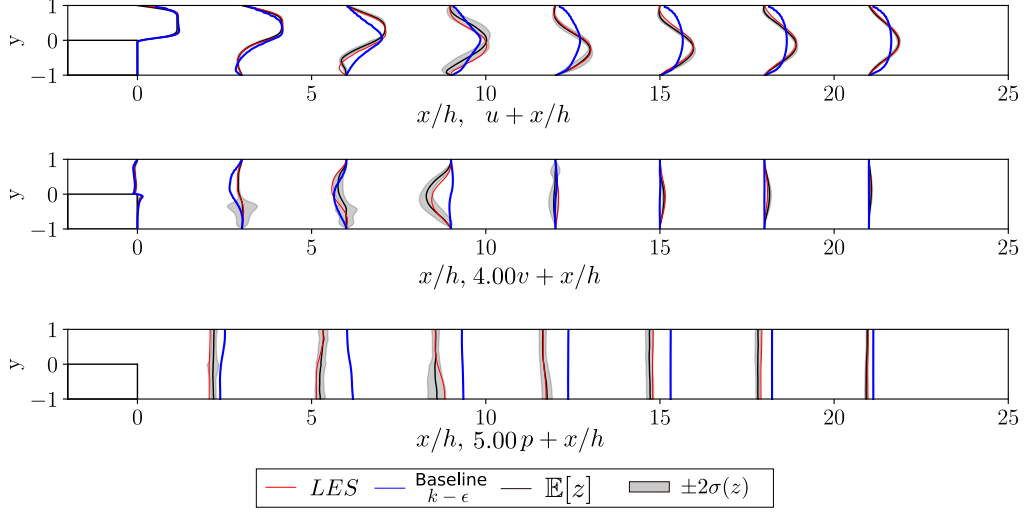


Figure 11: Section plots at different locations x/h comparing the LES and *Baseline* RANS mean fields with the posterior predictive mean (solid black line) and $\pm 2 \times$ standard deviation (shaded area) for the test case with $Re = 500$. **top** - velocity in x -direction (u), **middle** - velocity in the y -direction (v), **bottom** - pressure (p). $\mathbb{E}[z]$ and $\sigma(z)$ depict the predictive posterior mean and standard deviation respectively.

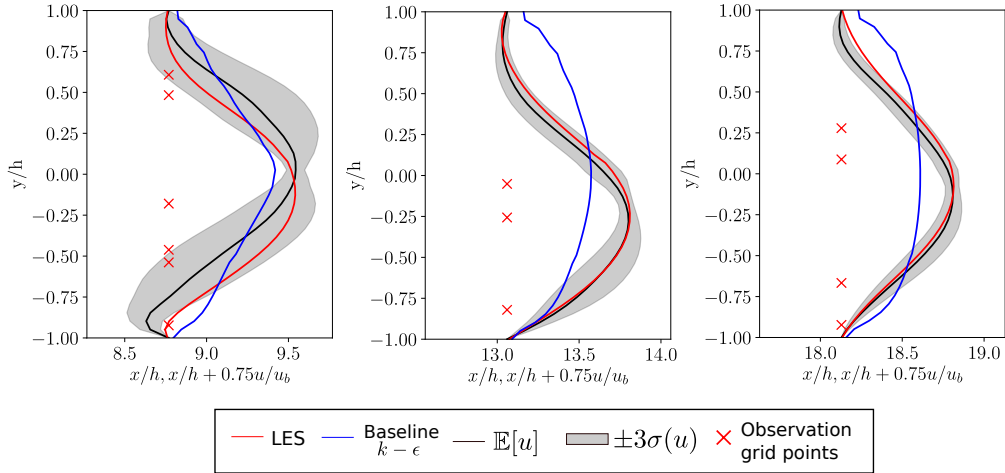


Figure 12: Section plots of the stream-wise velocity u at three different x/h locations for the test case with $Re = 500$. In addition, the points where training observations were available are depicted with red crosses. $\mathbb{E}[u]$ and $\sigma(u)$ depict the predictive posterior mean and standard deviation respectively.

prior in order to identify the regions in the problem domain where the parametric closure is insufficient and in order to quantify the stochastic correction to the Reynolds stress tensor. We have demonstrated how the model can be trained using sparse, indirect data, namely mean velocities/pressures in contrast to the majority of pertinent efforts that require direct, RS data. While the training data in our illustrations arose from a higher-fidelity model, one can readily envision

using experimental observations as well.

In order to enable inference and learning tasks, we developed a differentiable RANS solver capable of providing parametric sensitivities. Such a differentiable solver was non-trivial owing to the complexity of the physical simulator and its stability issues. The lack of such numerical tools has proven to be a significant barrier for intrusive, physics-based, data-driven models in turbulence [26]. This differentiable solver was utilized in the context of a Stochastic Variational Inference (SVI) scheme that employs Monte Carlo estimates of the ELBO derivatives in conjunction with the reparametrization trick and stochastic gradient ascent. We demonstrated how probabilistic predictive estimates can be computed for all output quantities of the trained RANS model and illustrated their accuracy on a separated flow in the backward facing step benchmark problem. In most cases, very good agreement with the reference values was achieved and in all cases these were enveloped by the credible intervals computed.

The proposed modeling framework offers several possibilities for extensions, some of which we discuss below:

- The indirect data i.e. velocities/pressures as in the Equation (22), could be complemented with direct, RS data at certain locations of the problem domain. This could be beneficial in improving the model’s predictive accuracy and generalization capabilities.
- The parametric closure model could benefit from non-local dependencies which could be enabled by convolutional or vector-cloud neural networks (VCNN) [93] with appropriate embedding of invariance properties.
- The dimensionality reduction of the stochastic discrepancy terms (Equation (19)) was based on a pre-selected and uniform division of the problem domain into subdomains. The accuracy of the model would certainly benefit from a learnable and adaptive scheme that would be able to focus on the areas where model deficiencies are most pronounced and stochastic corrections are most needed.

Acknowledgements

We extend our sincere thanks to Jigar Parekh for his valuable guidance in the generation of the LES data and to Maximilian Rixner for his assistance in implementing the forward solver. We are also thankful to Nicholas Geneva and Niklas Fehn for their valuable discussions that enriched this work. Our sincere gratitude is extended to the anonymous reviewers, whose insightful feedback greatly enhanced the quality of our manuscript.

Appendix A. Differentiable RANS solver

In the present study, the RANS equations (Equation (7)) are numerically solved using the finite element discretization, implemented in the open source package FEniCS [87]. The discrete equations are obtained by representing the solution and test functions in appropriate finite dimensional function spaces. In particular, we employed the standard Taylor-Hood pair of basis functions with polynomial degree one for the pressure interpolants and two for the velocities. This choice is made to avoid stability issues potentially arising from the interaction between the momentum and continuity equations.

The turbulence scaling terms, k and ϵ in Equation (17), are obtained by solving the respective standard transport equations [2, 52]. Symmetry is enforced in the RS tensor, i.e. τ_{xy} and τ_{yx} are identical without any redundancy in the representation. The discretized system is solved with damped Newton's method. For robustness and global convergence, pseudo-time stepping is used with the backward Euler discretization [94]. As the Reynolds number is increased, the convection term dominates, leading to stability [95]. This elicits a need to add stabilization terms to the weak form, such as the least-square stabilization, according to which the weighted square of the strong form is added to the weak form residual. However, these extra terms have to be chosen carefully in order not to compromise the correctness of the approximate solution. Classically, researchers added artificial diffusion terms or a numerical diffusion by using upwind scheme for the convection term instead of central diffusion. The extra infused term corrupted the solution quality. To avoid this, in practice, it is common to use schemes like Streamline-Upwind Petrov-Galerkin method (SUPG) and Galerkin Least Squares (GLS). In the present study, we have utilized a self-adjoint numerical stabilisation scheme which is an extension of Galerkin Least Squares (GLS) Stabilisation called Galerkin gradient least square method [96]. This amounts to adding a stabilization term to the residual weak form. For additional details, interested readers are referred to [96, 95].

Appendix B. Adjoint Formulation and Estimation of the Gradient of the ELBO

As discussed in Section 2.2.4, the SVI framework advocated, in combination with the reparametrization trick, requires derivatives of the ELBO with respect to the variables which we summararily denoted by $\boldsymbol{\eta} = \{\boldsymbol{\theta}, \boldsymbol{\Lambda}, \mathbf{E}_\tau^{(1:M)}\}$, i.e. (as in Equation (31)):

$$\nabla_{\boldsymbol{\xi}} \mathcal{F}(\boldsymbol{\xi}) = \mathbb{E}_{q(\boldsymbol{\phi})} \left[\nabla_{\boldsymbol{\xi}} g_{\boldsymbol{\xi}}(\boldsymbol{\phi}) \nabla_{\boldsymbol{\eta}} \left(\log p(\mathcal{D}, \boldsymbol{\eta}) - \log q_{\boldsymbol{\xi}}(\boldsymbol{\eta}) \right) \right], \quad (\text{B.1})$$

where from Equation (23):

$$\begin{aligned} \log p(\mathcal{D}, \boldsymbol{\eta}) &= \log \left(p(\mathcal{D} \mid \boldsymbol{\theta}, \mathbf{E}_\tau^{(1:M)}) p(\mathbf{E}_\tau^{(1:M)} \mid \boldsymbol{\Lambda}) p(\boldsymbol{\theta}) p(\boldsymbol{\Lambda}) \right) \\ &= \left(\sum_{m=1}^M \log p(\hat{\mathbf{z}}^{(m)} \mid \boldsymbol{\theta}, \mathbf{E}_\tau^{(m)}) + \log p(\mathbf{E}_\tau^{(m)} \mid \boldsymbol{\Lambda}) \right) \\ &\quad + \log p(\boldsymbol{\theta}) + \log p(\boldsymbol{\Lambda}). \end{aligned} \quad (\text{B.2})$$

The form of the (log-)priors $p(\mathbf{E}_\tau^{(m)} \mid \boldsymbol{\Lambda})$ (Equation (20)), $p(\boldsymbol{\theta})$ (Equation (18)), $p(\boldsymbol{\Lambda})$ (Equation (21)) as well as of the approximate posterior $q_{\boldsymbol{\xi}}(\boldsymbol{\eta})$ (Equations (26) and (27), (28), (29)) suggest that most of these derivatives can be analytically computed with the exception of the ones involving the log-likelihoods, i.e.:

$$\ell^{(m)}(\boldsymbol{\theta}, \mathbf{E}_\tau^{(m)}) = \log p(\hat{\mathbf{z}}^{(m)} \mid \boldsymbol{\theta}, \mathbf{E}_\tau^{(m)}). \quad (\text{B.3})$$

This is because each of these terms depends implicitly on θ , $\mathbf{E}_\tau^{(m)}$ through the output of the RANS solver $\mathbf{z}(\theta, \boldsymbol{\epsilon}_\tau^{(m)} = \mathbf{W}\mathbf{E}_\tau^{(m)})$ with the closure model for the discretized RS tensor field suggested by Equation (13) i.e. $\boldsymbol{\tau} = \boldsymbol{\tau}_\theta(\mathbf{u}) + \mathbf{W}\mathbf{E}_\tau^{(m)}$. In view of the governing equations (Equation (12)), we explain below how adjoint equations can be formulated that enable efficient computation of the aforementioned derivatives of the log-likelihoods.

In particular, and if we drop the superscript m for each term in the log-likelihood in order to simplify the notation, we formulate a Lagrangian with the help of a vector $\boldsymbol{\lambda}$ of Lagrangian multipliers, i.e.:

$$\mathcal{L} = \ell + \boldsymbol{\lambda}^T (\mathcal{G}(\mathbf{z}) - \mathbf{B}\boldsymbol{\tau}), \quad (\text{B.4})$$

where \mathcal{G} , \mathbf{B} , $\boldsymbol{\tau}$ and \mathbf{z} are as defined in Section (2.2). Differentiating with respect to $\boldsymbol{\tau}$ yields:

$$\begin{aligned} \frac{d\mathcal{L}}{d\boldsymbol{\tau}} &= \frac{\partial \ell}{\partial \mathbf{z}} \frac{d\mathbf{z}}{d\boldsymbol{\tau}} + \frac{d\boldsymbol{\lambda}^T}{d\boldsymbol{\tau}} (\mathcal{G}(\mathbf{z}) - \mathbf{B}\boldsymbol{\tau}) + \boldsymbol{\lambda}^T \left(\frac{\partial \mathcal{G}}{\partial \mathbf{z}} \frac{d\mathbf{z}}{d\boldsymbol{\tau}} - \mathbf{B} \right) \\ &= \left(\frac{\partial \ell}{\partial \mathbf{z}} + \boldsymbol{\lambda}^T \frac{\partial \mathcal{G}}{\partial \mathbf{z}} \right) \frac{d\mathbf{z}}{d\boldsymbol{\tau}} - \boldsymbol{\lambda}^T \mathbf{B}. \end{aligned} \quad (\text{B.5})$$

We select $\boldsymbol{\lambda}^T$ so that the first term in parentheses vanishes, i.e. :

$$\frac{\partial \ell}{\partial \mathbf{z}} + \boldsymbol{\lambda}^T \frac{\partial \mathcal{G}}{\partial \mathbf{z}} = 0 \quad \text{or,} \quad \left(\frac{\partial \mathcal{G}}{\partial \mathbf{z}} \right)^T \boldsymbol{\lambda} = - \left(\frac{\partial \ell}{\partial \mathbf{z}} \right)^T. \quad (\text{B.6})$$

The linear system of equations was solved using a direct LU solver. The vector $\boldsymbol{\lambda}$ found was substituted in Equation (B.5) in order to obtain the desired gradient which is given by:

$$\frac{d\mathcal{L}}{d\boldsymbol{\tau}} = \frac{d\ell}{d\boldsymbol{\tau}} = -\boldsymbol{\lambda}^T \mathbf{B}. \quad (\text{B.7})$$

Subsequently, and by application of the chain rule we can obtain derivatives with respect to θ as:

$$\frac{d\ell}{d\theta} = \underbrace{\frac{\partial \ell}{\partial \boldsymbol{\tau}}}_{\text{Adjoint model}} \underbrace{\frac{\partial \boldsymbol{\tau}}{\partial \theta}}_{\text{NN auto-diff}}, \quad (\text{B.8})$$

where $\partial \boldsymbol{\tau} / \partial \theta$ was efficiently computed by back-propagation, which is a reverse accumulation automatic differentiation algorithm for deep neural networks that applies the chain rule on a per-layer basis. We note that since the parameters θ are common for each likelihood $\ell^{(m)}$ the aforementioned terms would need to be added as per Equation (B.2).

Similarly by chain rule, the gradient with respect to the vector \mathbf{E}_τ is given by:

$$\frac{d\ell}{d\mathbf{E}_\tau} = \mathbf{W}^T \frac{d\ell}{d\boldsymbol{\tau}}. \quad (\text{B.9})$$

We note finally that the expectations involved in the ELBO and its gradient (Equation (31)) are

approximated by Monte Carlo i.e.:

$$\mathcal{F}(\xi) \approx \frac{1}{K} \left(\sum_{k=1}^K \left(\sum_{m=1}^M \ell^{(m)}(\theta, \mathbf{E}_\tau^{(m,k)}) + \log p(\mathbf{E}_\tau^{(m,k)} | \Lambda) \right) + \log p(\theta) + \log p(\Lambda) - \log q_\xi(\theta, \Lambda, \mathbf{E}_\tau^{(m,k)}) \right), \quad (\text{B.10})$$

where:

$$\phi^{(m,k)} \sim \mathcal{N}(\mathbf{0}, \mathbf{I}), \quad \mathbf{E}_\tau^{(m,k)} = g_\xi(\phi^{(m,k)}), \quad (\text{B.11})$$

and:

$$\nabla_\xi \mathcal{F}(\xi) \approx \frac{1}{K} \sum_{k=1}^K \nabla_\xi g_\xi(\phi^{(k)}) \nabla_\eta (\log p(\mathcal{D}, \eta^{(k)}) - \log q_\xi(\eta^{(k)})), \quad (\text{B.12})$$

where $\eta^{(k)} = g_\xi(\phi^{(k)})$.

References

- [1] I. Marusic, S. Broomhall, Leonardo da vinci and fluid mechanics, *Annual Review of Fluid Mechanics* 53 (1) (2021) 1–25. doi:10.1146/annurev-fluid-022620-122816.
- [2] S. B. Pope, *Turbulent flows*, Cambridge university press, 2000.
- [3] J. Slotnick, A. Khodadoust, J. Alonso, D. Darmofal, CFD Vision 2030 Study: A Path to Revolutionary Computational Aerosciences, NNASA/CR-2014-218178 (2014).
- [4] S. L. Brunton, B. R. Noack, P. Koumoutsakos, Machine learning for fluid mechanics, *Annual Review of Fluid Mechanics* 52 (2020) 477–508.
- [5] R. Vinuesa, S. L. Brunton, Emerging trends in machine learning for computational fluid dynamics, *Computing in Science & Engineering* 24 (5) (2022) 33–41.
- [6] D. Lucor, A. Agrawal, A. Sergent, Simple computational strategies for more effective physics-informed neural networks modeling of turbulent natural convection, *Journal of Computational Physics* 456 (2022) 111022, publisher: Elsevier Inc. doi:10.1016/j.jcp.2022.111022.
- [7] K. Duraisamy, Perspectives on Machine Learning-augmented Reynolds-averaged and Large Eddy Simulation Models of Turbulence, *Physical Review Fluids* 6 (5) (2021) 050504, arXiv:2009.10675 [physics]. doi:10.1103/PhysRevFluids.6.050504.
- [8] K. Duraisamy, G. Iaccarino, H. Xiao, Turbulence modeling in the age of data, *Annual Review of Fluid Mechanics* 51 (2019) 357–377.
- [9] T. A. Oliver, R. D. Moser, Bayesian uncertainty quantification applied to RANS turbulence models, in: *Journal of Physics: Conference Series*, Vol. 318, Institute of Physics Publishing, 2011, p. 042032. doi:10.1088/1742-6596/318/4/042032.
- [10] E. J. Parish, K. Duraisamy, A paradigm for data-driven predictive modeling using field inversion and machine learning, *Journal of Computational Physics* 305 (2016) 758–774.
- [11] A. P. Singh, S. Medida, K. Duraisamy, Machine-learning-augmented predictive modeling of turbulent separated flows over airfoils, *AIAA journal* 55 (7) (2017) 2215–2227.
- [12] B. D. Tracey, K. Duraisamy, J. J. Alonso, A machine learning strategy to assist turbulence model development, in: *53rd AIAA aerospace sciences meeting*, 2015, p. 1287.
- [13] H. Xiao, J.-L. Wu, J.-X. Wang, R. Sun, C. Roy, Quantifying and reducing model-form uncertainties in reynolds-averaged navier–stokes simulations: A data-driven, physics-informed bayesian approach, *Journal of Computational Physics* 324 (2016) 115–136.
- [14] Z. J. Zhang, K. Duraisamy, Machine learning methods for data-driven turbulence modeling, in: *22nd AIAA computational fluid dynamics conference*, 2015, p. 2460.
- [15] J. Ling, A. Kurzawski, J. Templeton, Reynolds averaged turbulence modelling using deep neural networks with embedded invariance, *Journal of Fluid Mechanics* 807 (2016) 155–166.
- [16] J. Ling, R. Jones, J. Templeton, Machine learning strategies for systems with invariance properties, *Journal of Computational Physics* 318 (2016) 22–35, publisher: Elsevier Inc. doi:10.1016/j.jcp.2016.05.003.
- [17] M. L. Kaandorp, R. P. Dwight, Data-driven modelling of the reynolds stress tensor using random forests with invariance, *Computers & Fluids* 202 (2020) 104497.

- [18] J.-X. Wang, J. Wu, J. Ling, G. Iaccarino, H. Xiao, A comprehensive physics-informed machine learning framework for predictive turbulence modeling, arXiv preprint arXiv:1701.07102 (2017).
- [19] M. Schmelzer, R. P. Dwight, P. Cinnella, Discovery of algebraic reynolds-stress models using sparse symbolic regression, *Flow, Turbulence and Combustion* 104 (2020) 579–603.
- [20] X.-L. Zhang, H. Xiao, X. Luo, G. He, Ensemble Kalman method for learning turbulence models from indirect observation data, *Journal of Fluid Mechanics* 949 (2022) A26, publisher: Cambridge University Press. doi: 10.1017/jfm.2022.744.
- [21] S. B. Pope, A more general effective-viscosity hypothesis, *Journal of Fluid Mechanics* 72 (2) (1975) 331–340.
- [22] N. Geneva, N. Zabararas, Quantifying model form uncertainty in reynolds-averaged turbulence models with bayesian deep neural networks, *Journal of Computational Physics* 383 (2019) 125–147.
- [23] S. Taghizadeh, F. D. Witherden, S. S. Girimaji, Turbulence closure modeling with data-driven techniques: physical compatibility and consistency considerations, *New Journal of Physics* 22 (9) (2020) 093023.
- [24] R. L. Thompson, L. E. B. Sampaio, F. A. de Bragança Alves, L. Thais, G. Mompean, A methodology to evaluate statistical errors in dns data of plane channel flows, *Computers & Fluids* 130 (2016) 1–7.
- [25] J. Wu, H. Xiao, R. Sun, Q. Wang, Reynolds-averaged navier–stokes equations with explicit data-driven reynolds stress closure can be ill-conditioned, *Journal of Fluid Mechanics* 869 (2019) 553–586.
- [26] K. Cranmer, J. Brehmer, G. Louppe, The frontier of simulation-based inference, *Proceedings of the National Academy of Sciences* 117 (48) (2020) 30055–30062.
- [27] D. A. Bezgin, A. B. Buhendwa, N. A. Adams, A fully-differentiable compressible high-order computational fluid dynamics solver, arXiv preprint arXiv:2112.04979 (2021).
- [28] B. List, L.-W. Chen, N. Thuerey, Learned turbulence modelling with differentiable fluid solvers: physics-based loss functions and optimisation horizons, *Journal of Fluid Mechanics* 949 (2022) A25.
- [29] K. Um, R. Brand, Y. R. Fei, P. Holl, N. Thuerey, Solver-in-the-loop: Learning from differentiable physics to interact with iterative pde-solvers, *Advances in Neural Information Processing Systems* 33 (2020) 6111–6122.
- [30] D. Kochkov, J. A. Smith, A. Alieva, Q. Wang, M. P. Brenner, S. Hoyer, Machine learning–accelerated computational fluid dynamics, *Proceedings of the National Academy of Sciences* 118 (21) (2021) e2101784118.
- [31] M. B. Giles, M. C. Duta, J.-D. Muller, N. A. Pierce, Algorithm developments for discrete adjoint methods, *AIAA journal* 41 (2) (2003) 198–205.
- [32] M. B. Giles, N. A. Pierce, An introduction to the adjoint approach to design, *Flow, turbulence and combustion* 65 (3) (2000) 393–415.
- [33] A. Jameson, Aerodynamic design via control theory, *Journal of scientific computing* 3 (1988) 233–260.
- [34] E. Parish, K. Duraisamy, Quantification of turbulence modeling uncertainties using full field inversion, in: 22nd AIAA Computational Fluid Dynamics Conference, 2015, p. 2459.
- [35] J. R. Holland, J. D. Baeder, K. Duraisamy, Towards Integrated Field Inversion and Machine Learning With Embedded Neural Networks for RANS Modeling, in: AIAA Scitech 2019 Forum, American Institute of Aeronautics and Astronautics, _eprint: <https://arc.aiaa.org/doi/pdf/10.2514/6.2019-1884>. doi:10.2514/6.2019-1884.
- [36] O. Bidar, P. He, S. Anderson, N. Qin, An Open-source Adjoint-based Field Inversion Tool for Data-driven RANS Modelling, 2022. doi:10.2514/6.2022-4125.
- [37] O. Brenner, P. Piroozmand, P. Jenny, Efficient assimilation of sparse data into rans-based turbulent flow simulations using a discrete adjoint method, *Journal of Computational Physics* 471 (2022) 111667.
- [38] I. B. H. Saïdi, M. Schmelzer, P. Cinnella, F. Grasso, Cfd-driven symbolic identification of algebraic reynolds-stress models, *Journal of Computational Physics* 457 (2022) 111037.
- [39] Y. Zhao, H. D. Akolekar, J. Weatheritt, V. Michelassi, R. D. Sandberg, Rans turbulence model development using cfd-driven machine learning, *Journal of Computational Physics* 411 (2020) 109413.
- [40] C. A. M. Ströfer, H. Xiao, End-to-end differentiable learning of turbulence models from indirect observations, *Theoretical and Applied Mechanics Letters* 11 (4) (2021) 100280.
- [41] E. J. Parish, K. Duraisamy, Non-markovian closure models for large eddy simulations using the mori-zwanzig formalism, *Physical Review Fluids* 2 (1) (2017) 014604.
- [42] J. A. Schaefer, A. W. Cary, M. Mani, P. R. Spalart, Uncertainty quantification and sensitivity analysis of sa turbulence model coefficients in two and three dimensions, in: 55th AIAA Aerospace Sciences Meeting, 2017, p. 1710.
- [43] H. Xiao, P. Cinnella, Quantification of model uncertainty in rans simulations: A review, *Progress in Aerospace Sciences* 108 (2019) 1–31.
- [44] J.-X. Wang, R. Sun, H. Xiao, Quantification of uncertainties in turbulence modeling: A comparison of physics-based and random matrix theoretic approaches, *International Journal of Heat and Fluid Flow* 62 (2016) 577–592.
- [45] M. Emory, J. Larsson, G. Iaccarino, Modeling of structural uncertainties in reynolds-averaged navier-stokes closures, *Physics of Fluids* 25 (11) (2013) 110822.
- [46] C. Gorié, G. Iaccarino, A framework for epistemic uncertainty quantification of turbulent scalar flux models for reynolds-averaged navier-stokes simulations, *Physics of Fluids* 25 (5) (2013) 055105.

- [47] W. N. Edeling, G. Iaccarino, P. Cinnella, Data-free and data-driven rans predictions with quantified uncertainty, *Flow, Turbulence and Combustion* 100 (3) (2018) 593–616.
- [48] R. L. Thompson, A. A. Mishra, G. Iaccarino, W. Edeling, L. Sampaio, Eigenvector perturbation methodology for uncertainty quantification of turbulence models, *Physical Review Fluids* 4 (4) (2019) 044603.
- [49] J.-L. Wu, J.-X. Wang, H. Xiao, J. Ling, A priori assessment of prediction confidence for data-driven turbulence modeling, *Flow, Turbulence and Combustion* 99 (2017) 25–46.
- [50] P.-S. Koutsourelakis, N. Zabaras, M. Girolami, Big data and predictive computational modeling, *Journal of Computational Physics* 321 (2016) 1252–1254.
- [51] P. M. Gresho, D. K. Gartling, J. Torczynski, K. Cliffe, K. Winters, T. Garratt, A. Spence, J. W. Goodrich, Is the steady viscous incompressible two-dimensional flow over a backward-facing step at $re=800$ stable?, *International Journal for Numerical Methods in Fluids* 17 (6) (1993) 501–541.
- [52] G. Alfonsi, Reynolds-Averaged Navier-Stokes Equations for Turbulence Modeling, *Applied Mechanics Reviews - APPL MECH REV* 62 (Jul. 2009). doi:10.1115/1.3124648.
- [53] S. E. Ahmed, S. Pawar, O. San, A. Rasheed, T. Iliescu, B. R. Noack, On closures for reduced order models—A spectrum of first-principle to machine-learned avenues, *Physics of Fluids* 33 (9) (2021) 091301, arXiv: 2106.14954. doi:10.1063/5.0061577.
- [54] O. San, R. Maulik, Neural network closures for nonlinear model order reduction (May 2017). doi:10.48550/arXiv.1705.08532.
- [55] W. Snyder, C. Mou, H. Liu, O. San, R. De Vita, T. Iliescu, Reduced Order Model Closures: A Brief Tutorial, arXiv:2202.14017 [physics]ArXiv: 2202.14017 (Feb. 2022).
- [56] B. E. Launder, B. I. Sharma, Application of the energy-dissipation model of turbulence to the calculation of flow near a spinning disc, *Letters in Heat and Mass Transfer* 1 (2) (1974) 131–137. doi:10.1016/0094-4548(74)90150-7.
- [57] D. C. Wilcox, Formulation of the $k-\omega$ turbulence model revisited, in: *AIAA Journal*, Vol. 46, 2008, pp. 2823–2838. doi:10.2514/1.36541.
- [58] D. C. Wilcox, et al., *Turbulence modeling for CFD*, Vol. 2, DCW industries La Canada, CA, 1998.
- [59] C. G. Speziale, On nonlinear $K-l$ and $K-\epsilon$ models of turbulence, *Journal of Fluid Mechanics* 178 (1987) 459–475. doi:10.1017/S0022112087001319.
- [60] T. Craft, B. Launder, K. Suga, Development and application of a cubic eddy-viscosity model of turbulence, *International Journal of Heat and Fluid Flow* 17 (2) (1996) 108–115.
- [61] B. E. Launder, G. J. Reece, W. Rodi, Progress in the development of a reynolds-stress turbulence closure, *Journal of fluid mechanics* 68 (3) (1975) 537–566.
- [62] T. B. Gatski, C. G. Speziale, On explicit algebraic stress models for complex turbulent flows, *Journal of fluid Mechanics* 254 (1993) 59–78.
- [63] S. S. Girimaji, Fully explicit and self-consistent algebraic reynolds stress model, *Theoretical and Computational Fluid Dynamics* 8 (6) (1996) 387–402.
- [64] S. E. Ahmed, S. Pawar, O. San, A. Rasheed, T. Iliescu, B. R. Noack, On closures for reduced order models—A spectrum of first-principle to machine-learned avenues, *Physics of Fluids* 33 (9), 091301 (09 2021). doi:10.1063/5.0061577.
- [65] J.-X. Wang, J.-L. Wu, H. Xiao, Physics-informed machine learning approach for reconstructing reynolds stress modeling discrepancies based on dns data, *Physical Review Fluids* 2 (3) (2017) 034603.
- [66] G. Iaccarino, A. A. Mishra, S. Ghili, Eigenspace perturbations for uncertainty estimation of single-point turbulence closures, *Physical Review Fluids* 2 (2) (2017). doi:10.1103/PhysRevFluids.2.024605.
- [67] A. A. Mishra, G. Iaccarino, Uncertainty estimation for reynolds-averaged navier-stokes predictions of high-speed aircraft nozzle jets, *AIAA Journal* 55 (11) (2017) 3999–4004. doi:10.2514/1.J056059.
- [68] C. M. Bishop, N. M. Nasrabadi, *Pattern recognition and machine learning*, Vol. 4, Springer, 2006.
- [69] M. E. Tipping, C. M. Bishop, Probabilistic principal component analysis, *Journal of the Royal Statistical Society Series B: Statistical Methodology* 61 (3) (1999) 611–622.
- [70] S. L. Brunton, J. L. Proctor, J. N. Kutz, Discovering governing equations from data by sparse identification of nonlinear dynamical systems, *Proceedings of the national academy of sciences* 113 (15) (2016) 3932–3937, publisher: National Acad Sciences.
- [71] L. Felsberger, P. Koutsourelakis, Physics-constrained, data-driven discovery of coarse-grained dynamics, *Communications in Computational Physics* 25 (5) (2019) 1259–1301. doi:10.4208/cicp.OA-2018-0174.
- [72] R. M. Neal, *Bayesian learning for neural networks*, Vol. 118, Springer Science & Business Media, 2012.
- [73] A. Wu, M. Park, O. Koyejo, J. W. Pillow, Sparse bayesian structure learning with dependent relevance determination prior, in: *Proceedings of the 27th International Conference on Neural Information Processing Systems - Volume 1, NIPS'14*, MIT Press, Cambridge, MA, USA, 2014, p. 1628–1636.
- [74] M. E. Tipping, The Relevance Vector Machine, in: S. A. Solla, T. K. Leen, K.-R. Müller (Eds.), *Advances in Neural Information Processing Systems 12*, MIT Press, 2000, pp. 652–658.

- [75] C. Bishop, Variational principal components, in: 1999 Ninth International Conference on Artificial Neural Networks ICANN 99. (Conf. Publ. No. 470), Vol. 1, 1999, pp. 509–514 vol.1, iISSN: 0537-9989. doi:10.1049/cp:19991160.
- [76] M. D. Hoffman, D. M. Blei, C. Wang, J. Paisley, Stochastic variational inference, *Journal of Machine Learning Research* (2013).
- [77] D. M. Blei, A. Kucukelbir, J. D. McAuliffe, Variational inference: A review for statisticians, *Journal of the American statistical Association* 112 (518) (2017) 859–877.
- [78] D. P. Kingma, J. Ba, Adam: A method for stochastic optimization, arXiv preprint arXiv:1412.6980 (2014).
- [79] D. P. Kingma, M. Welling, Auto-encoding variational bayes, arXiv preprint arXiv:1312.6114 (2013).
- [80] J. M. Bardsley, Gaussian markov random field priors for inverse problems, *Inverse Problems and Imaging* 7 (2) (2013) 397–416. doi:10.3934/ipi.2013.7.397.
- [81] P. M. Nadge, R. Govardhan, High reynolds number flow over a backward-facing step: structure of the mean separation bubble, *Experiments in fluids* 55 (1) (2014) 1–22.
- [82] F. Pioch, J. H. Harmening, A. M. Müller, F.-J. Peitzmann, D. Schramm, O. e. Moctar, Turbulence Modeling for Physics-Informed Neural Networks: Comparison of Different RANS Models for the Backward-Facing Step Flow, *Fluids* 8 (2) (2023) 43, number: 2 Publisher: Multidisciplinary Digital Publishing Institute. doi:10.3390/fluids8020043.
- [83] H. Jasak, A. Jemcov, Z. Tukovic, et al., Openfoam: A c++ library for complex physics simulations, in: *International workshop on coupled methods in numerical dynamics*, Vol. 1000, 2007, pp. 1–20.
- [84] F. Nicoud, F. Ducros, Subgrid-scale stress modelling based on the square of the velocity gradient tensor, *Flow, turbulence and Combustion* 62 (3) (1999) 183–200.
- [85] L. Engelmann, M. Ihme, I. Wlokas, A. Kempf, Towards the suitability of information entropy as an les quality indicator, *Flow, Turbulence and Combustion* (2021) 1–33.
- [86] I. Celik, Z. Cehreli, I. Yavuz, Index of resolution quality for large eddy simulations (2005).
- [87] M. Alnæs, J. Blechta, J. Hake, A. Johansson, B. Kehlet, A. Logg, C. Richardson, J. Ring, M. E. Rognes, G. N. Wells, The fenics project version 1.5, *Archive of Numerical Software* 3 (100) (2015).
- [88] S. K. Mitusch, S. W. Funke, J. S. Dokken, dolfin-adjoint 2018.1: automated adjoints for fenics and firedrake, *Journal of Open Source Software* 4 (38) (2019) 1292.
- [89] E. Bingham, J. P. Chen, M. Jankowiak, F. Obermeyer, N. Pradhan, T. Karaletsos, R. Singh, P. Szerlip, P. Horsfall, N. D. Goodman, Pyro: Deep universal probabilistic programming, *The Journal of Machine Learning Research* 20 (1) (2019) 973–978.
- [90] A. Paszke, S. Gross, F. Massa, A. Lerer, J. Bradbury, G. Chanan, T. Killeen, Z. Lin, N. Gimelshein, L. Antiga, et al., Pytorch: An imperative style, high-performance deep learning library, *Advances in neural information processing systems* 32 (2019).
- [91] B. F. Armaly, F. Durst, J. Pereira, B. Schönung, Experimental and theoretical investigation of backward-facing step flow, *Journal of fluid Mechanics* 127 (1983) 473–496.
- [92] G. Biswas, M. Breuer, F. Durst, Backward-facing step flows for various expansion ratios at low and moderate reynolds numbers, *J. Fluids Eng.* 126 (3) (2004) 362–374.
- [93] J. Han, X.-H. Zhou, H. Xiao, Vcnn-e: A vector-cloud neural network with equivariance for emulating reynolds stress transport equations, arXiv preprint arXiv:2201.01287 (2022).
- [94] P. Deuffhard, *Newton methods for nonlinear problems: affine invariance and adaptive algorithms*, Vol. 35, Springer Science & Business Media, 2005.
- [95] J. Donea, A. Huerta, *Finite element methods for flow problems*, John Wiley & Sons, 2003.
- [96] L. P. Franca, E. G. D. Do Carmo, The galerkin gradient least-squares method, *Computer Methods in Applied Mechanics and Engineering* 74 (1) (1989) 41–54.